A Two-Dimensional Numerical Investigation of the Interaction between Sea Breezes and Deep Convection over the Florida Peninsula

MELVILLE E. NICHOLLS, ROGER A. PIELKE AND WILLIAM R. COTTON

Department of Atmospheric Science, Colorado State University, Fort Collins, Colorado

(Manuscript received 17 November 1989, in final form 6 August 1990)

ABSTRACT

Deep convection initiated by sea breezes over the Florida peninsula is simulated using a two-dimensional nonhydrostatic model. Reasonable agreement is obtained between model results and observations for the three types of undisturbed days classified by Blanchard and López. The convergence of the east and west coast sea breezes is the primary control on the timing and location of rapid convective development, and this is mainly determined by the low-level winds. The simulated convection is spatially concentrated and does not produce an extensive stratiform region.

Sensitivity tests are performed for a variety of wind and thermodynamic profiles, and for different soil moisture contents. During the early stages of these simulations, small convective cells develop in between the sea-breeze fronts. As the outer cells at the sea-breeze fronts deepen these smaller cells are suppressed. Typically, during the midafternoon a new cell explosively develops in between the sea-breeze fronts and the outer cells usually decay, although merger occasionally occurs. The decay of convection, subsequent to this rapid development, can generate very deep horizontally propagating gravity waves. A considerable amount of the convective available potential energy released, and associated subsidence warming is carried away from the convective region by these deep gravity-wave modes having a horizontal propagation speed much larger than the ambient winds. Model output is analyzed to examine the precipitation patterns, heat and moisture budgets, radiational heating and momentum transports.

1. Introduction

The influence of sea breezes on the development of convection over the Florida peninsula has been the subject of numerous observational studies (Byers and Rodebush 1948; Gentry and Moore 1954; Frank et al. 1967; Pielke and Cotton 1977; Burpee and Lahiff 1984; Blanchard and Lopez 1985; and others). These investigations have emphasized the role that the sea-breeze convergence zones play in initiating and organizing convection. Three-dimensional modeling efforts by Pielke (1974), and Pielke and Mahrer (1978) provide further evidence that the sea breeze is the dominant control on the preferred location of cumulonimbus over south Florida on synoptically undisturbed days. In this paper, we include moist processes and investigate the interaction between the sea-breeze circulation and deep convection using a nonhydrostatic model. Due to computational limitations, the fully three-dimensional explicit simulation of convection over the whole of the Florida peninsula is not yet feasible. Nicholls and Weissbluth (1988) investigated the differences between a two-dimensional simulation of a tropical squall line and a simulation that allowed three-dimensionality on the scale of convective elements. Although there were some differences, the basic structure of the system appeared reasonably well simulated in two dimensions. Furthermore, Tripoli and Cotton (1989a,b) showed that a two-dimensional model with explicit convection could simulate the observed scenario of an orogenic mesoscale convective system. Hence, in this investigation, two-dimensional simulations are carried out that should provide a basis for future, more complex, three-dimensional studies.

The environmental wind profiles used in this study are based mainly on the results of Blanchard and Lopez (1985) who classified undisturbed days into three types. Radar echoes and the synoptic situation for these types are described in detail by Blanchard and Lopez (1985) and the reader is referred to their paper for a complete discussion of the observations. The Type 1 situation is characterized by major development of convection along both coasts due to low-level uplift at the sea-breeze fronts. The east coast convection moves inland fairly rapidly, whereas the west coast convection moves more slowly. Merging of the radar echoes usually occurs west of the center of the peninsula. The convection is strongest in the interior of the peninsula and diminishes in the early evening. Type 2 days start out in a fashion similar to the Type 1 days. However, the east coast convection moves inland very quickly, whereas the west coast convection is very weak. Later in the afternoon,

Corresponding author address: Dr. Melville Nicholls, Dept. of Atmospheric Science, Colorado State University, Fort Collins, CO 80523.

© 1991 American Meteorological Society

1500–1800 EDT, convection becomes more widespread, but is concentrated in the western half of the peninsula as the east coast and west coast sea-breeze fronts merge near the west coast. It eventually moves over the sea. On Type 3 days, convection starts earlier than on Type 1 or Type 2 days. In this case, it is the west coast convection that moves inland quickly, eventually merging with the convection on the east coast. Type 3 days exhibit a higher echo area coverage and dissipation takes place later in the day.

Blanchard and Lopez suggest that the wind profile is the main factor differentiating these types. The typical wind field for Type 1 days has an easterly component. This would have the effect of causing the east coast sea breeze to move inland during the day, while the west coast sea breeze remains anchored to a position just slightly inland. This feature has been noted by Gentry and Moore (1954), and Frank et al. (1967), among others. A modeling investigation by Pielke (1974) substantiated the conclusion that an easterly component of wind causes the east coast sea breeze to move inland more rapidly than the west coast sea breeze. Type 2 days are characterized by a stronger easterly component of wind than on Type 1 days, accounting for the more rapid inland penetration of the east coast sea breeze. On the other hand, Type 3 days are characterized by a westerly component of wind, so that it is the west coast sea breeze that propagates inland more quickly. Blanchard and Lopez also found that on Type 2 days there is significantly less midlevel moisture than for the other types and that the lapse rates tend to be more stable.

The goals of this study are 1) to determine whether a nonhydrostatic model is capable of reproducing the observed evolution of convection over the Florida peninsula during undisturbed days; 2) to ascertain if it is predominantly the wind profile that is responsible for the characteristic types classified by Blanchard and Lopez (1985); 3) to determine the sensitivity of the deep convection to variations of the wind and thermodynamic profiles and to soil moisture content; 4) to investigate the upscale development from shallow cumulus to cumulonimbus; 5) to determine the environmental changes produced by the deep convection; and 6) to assess the importance of radiational effects.

Initiation of convection by a diurnally varying sea breeze is a natural mechanism, in contrast to perturbing a horizontally homogeneous environment, which is the procedure used in most previous modeling studies of deep convection. The model used in this study includes parameterizations of both liquid and ice phase microphysical processes, surface layer fluxes, and short- and longwave radiative effects. The cloud model used in this study is discussed in section 2. A description of the experiments is given in section 3. In sections 4 and 5 the results and conclusions are presented, respectively.

2. The model

The cloud model used in this study is the Colorado State University Regional Atmospheric Modeling System (RAMS). The model contains a full set of nonhydrostatic compressible dynamic equations, a thermodynamic equation, and a set of microphysics equations for water- and ice-phase clouds and precipitation.

The surface parameterization of vertical heat, vapor, and momentum fluxes is based on the Louis (1979) scheme. The scheme provides fluxes as a function of vertical gradients of temperature, moisture, and horizontal velocity between the top of the surface layer and the surface. The height of the surface layer is taken as the height of the first theta level above the surface. While the horizontal velocity is assumed to vanish at the surface, values of temperature and moisture are predicted from the upper-most level of a multilevel prognostic soil model developed by McCumber and Pielke (1981) and modified for RAMS by Tremback and Kessler (1985). For the simulations discussed in this article, eight levels are used for the prognostic soil scheme, which extends to 68 cm below the surface. For simplicity, a homogeneous, sandy clay loam-type is used for the soil layer and a fairly dry volumetric moisture content is assumed. The model includes transports of heat and moisture from the sea.

The longwave and shortwave radiation parameterization developed by Chen and Cotton (1983) is employed. The longwave scheme takes into account both the effects of clear-air and cloudy-air absorption. Within clear air, the effects of both water-vapor and carbon dioxide absorption are predicted. The parameterization of cloud effects is based on an empirically derived scheme proposed by Stephens (1978a,b). The shortwave parameterization considers effects of absorption, reflection, and scattering in both clear and cloudy conditions. Absorption by both water vapor and ozone are considered. Within a cloudy atmosphere, shortwave absorption is based on Stephens (1978a,b).

The model includes parameterizations of cloud water, rainwater, pristine ice crystals, snow and graupel. All hydrometeors in a cloud have to develop from nucleated cloud water or ice water. The concentration of activated cloud droplets is specified by the model user as a climatologically derived input parameter. Primary nucleation of pristine ice crystals is based on the degree of supercooling (Fletcher 1962), supersaturation (Huffman and Vali 1973), and contact nucleation. Secondary nucleation by the Hallet–Massop ice multiplication process is represented by a parameterization developed by Gordon and Marwitz (1981). All microphysical categories can grow by vapor deposition. The governing equation for vapor depositional growth is derived in standard cloud physics texts (Byers 1965; Pruppacher and Klett 1978; Ludlam 1980). Vapor deposition can change due to ventilation as the fall speed

of a particle increases and this is based on a formulation used by Cotton et al. (1982). The surface temperature of hydrometeors is deduced by assuming thermal equilibrium such that the rate of heat released by vapor deposition and freezing is balanced by the rate of diffusion of heat from the particle surface. Growth by collision and coalescence can occur both with other categories and within the same category. The autoconversion of cloud droplets to rain is based on a threshold average diameter in the droplet distribution (Manton and Cotton 1977).

Growth of pristine ice crystals by vapor deposition, riming, or self-collection results in a conversion to the snow category. The snow category can grow through vapor deposition, aggregation, and riming. Graupel is initiated by contact freezing of raindrops colliding with ice particles and from conversion of heavily rimed snow. Graupel can then grow by collection of rain or cloud droplets through the dry or wet growth process and by collection of pristine ice crystals and snow. Both snow and graupel can convert to rain through melting. For the pristine ice crystal, snow, and graupel categories, the number concentration of ice particles is predicted. Pristine ice is monodispersed, whereas snow and graupel are distributed according to the inverse exponential distribution function (Marshall–Palmer), with the characteristic radius a determined variable. The Marshall–Palmer distribution is also employed for the raindrop distribution and a mean characteristic radius is specified.

Vertical and horizontal turbulent eddy mixing is modeled by a first-order eddy viscosity closure scheme that includes a buoyancy enhancement term (Hill 1974). The Coriolis force is incorporated in the manner described by Tripoli and Cotton (1989a). The time-differencing scheme is similar to that reported by Klemp and Wilhelmson (1978), and modified by Tripoli and Cotton (1980). Acoustic terms are integrated with a small time step and low-frequency terms with a large time step. The equations are solved on a standard velocity staggered grid described by Tripoli and Cotton (1982).

The horizontal grid spacing used for the two-dimensional simulations is 1 km and the vertical resolution 400 m at the surface, which is gradually stretched to 1 km at the top of the model. The domain size is 400 km in the horizontal and 22 km in the vertical, and assumes a latitude of 26.5°N. There are 32 vertical grid points above the soil layer. Since the grid is staggered, the first theta level above the surface is at 200 m, which is taken as the top of the surface layer. The land surface is 200 km in width surrounded by 100 km of water on either side. A rigid lid is used for the upper boundary condition. A weak dissipative layer 7 km in depth is included at the top of the domain to reduce reflection of gravity waves from the upper boundary. The lateral boundaries incorporate a mesoscale compensation region (MCR; see Tripoli and Cotton 1982). The MCR is included to provide a large-scale mass balance adjustment due to circulation trends generated within the interior model domain. Lateral boundaries of the domain additionally incorporate the Klemp–Lilly (1978) radiation boundary condition to allow propagation of gravity waves through the interior model walls. In order that any tendency for small cells to develop is not inhibited by the use of a horizontally homogeneous basic state, small randomly specified temperature perturbations (<0.2°C) are initially introduced into the first level above the surface. The set of random numbers is identical for all experiments except for a simulation discussed in section 5.

3. Description of experiments

The thermodynamic profile used in these experiments is the 0700 EST Miami sounding for 17 July 1973 during FACE (Florida Area Cumulus Experiment). This day has also been investigated by Tripoli and Cotton (1980) who simulated an individual cumulonimbus, and by Song (1986) who modeled the sea-breeze circulations over south Florida using a 22-km horizontal grid and a cumulus parameterization. The thermodynamic sounding is shown in Fig. 1, which also shows alterations to the temperature and moisture profiles used in experiments to be discussed later.

As mentioned in the Introduction, the choice of wind profiles is motivated mainly by the results of Blanchard and Lopez (1985), who classified undisturbed days into three types. The wind component perpendicular to the coast for these three types is shown in Fig. 2. The wind profile observed at Miami 0700 EST for 17 July 1973 is similar to the Type 2 situation, whereas an inland sounding at the FACE Central Site at 0900 EST, is more like the Type 1 case (see Tripoli and Cotton 1980, Fig. 3). In addition to these three types, we include simulations for no initial winds and for the profiles shown in Fig. 3. One of these profiles has moderate shear beneath 2.5 km and no shear aloft, and the other has a weak low-level jet. Wind shears are typically weak below the upper troposphere on undisturbed days over the Florida peninsula, so the changes made to the wind profile are kept fairly modest.

Variations in moisture content were found by Blanchard and Lopez for the three types they classified. In particular, Type 3 was considerably more moist at midlevels than Type 2. Simulations were carried out for moister soundings indicated by the dashed and dotted lines in Fig. 1. Experiments using the moister sounding indicated by the dashed line will be discussed for both Type 1 and Type 3 wind profiles. For the very moist sounding indicated by the dotted line the Type 3 wind profile was used. A simulation was also performed for a modified boundary layer and for the Type 1 wind profile. For this case, the surface temperature

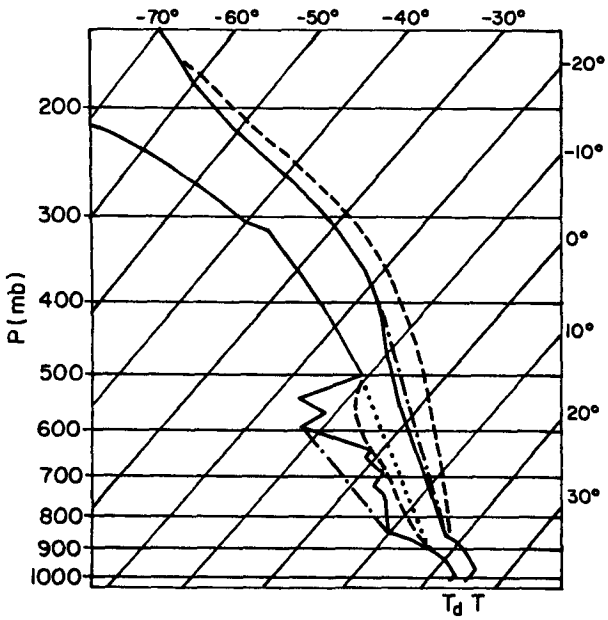

FIG. 1. Initial temperature and dewpoint temperature. The solid lines show the control environment. A moist adiabat is indicated by a dashed line. Also shown are modifications to the control environment: for the moist environment used in experiments 7 and 8 the dewpoint temperature curve is modified as shown by the dashed line. For the very moist environment used in experiment 9 the dewpoint temperature curve is modified as shown by the dotted line. For the more stable environment used in experiment 11 the temperature curve is modified as shown by the dash–dot line. For the more stable, dry midlevels environment used in experiment 12 the temperature and dewpoint temperature are modified as shown by the dash–dot lines.

was increased by 2°C and the surface moisture by 1.0 g kg^{-1}. These perturbations linearly decrease to zero at a height of 1 km. According to Blanchard and López, there is a tendency for the environment on Type 2 days to be more stable and to have drier midlevels than the other cases. Therefore, experiments were made both for the more stable sounding indicated by the dash–dot line in Fig. 1 and also in combination with the drier sounding shown in this figure (also indicated by a dash–dot line). Sensitivity tests to the surface fluxes were carried out by specifying a very dry and a very moist soil layer (10% and 80% of the maximum volumetric moisture content, respectively). Finally, a simulation was run without any microphysics for the Type 1 wind profile.

A list of the experiments is given in Table 1. Additional simulations that will not be discussed in detail were made for the moister sounding (indicated by the dashed line in Fig. 1) for the Type 2 wind profile, no wind, low-level shear, low-level jet, modified boundary layer, dry and moist soil cases. These experiments were carried out to determine if the trends found for the control sounding would also be found for a moister midlevel environment. They will be discussed briefly in section 4b.

The simulations are begun at 0800 EST and end at 2000 EST, except for experiment 1 (the Type 1 wind profile case) for which the run was continued to midnight. A sensitivity test of starting the simulation at sunrise instead of at 0800 EST indicated only small differences to the sea-breeze circulation.

4. Results

a. Description of individual cases

1) TYPE 1 WIND PROFILE

The thermodynamic and wind profiles used in this experiment are shown by the solid lines in Figs. 1 and 2, respectively. As the land surface warms due to radiative heating, sea breezes form on both coasts and propagate inland. Weak convection starts to develop

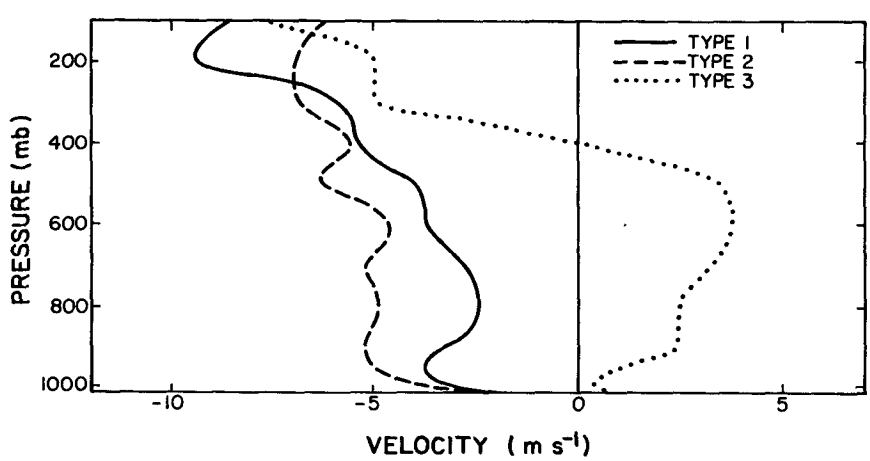

FIG. 2. Initial wind profiles for Type 1, Type 2, and Type 3 days.

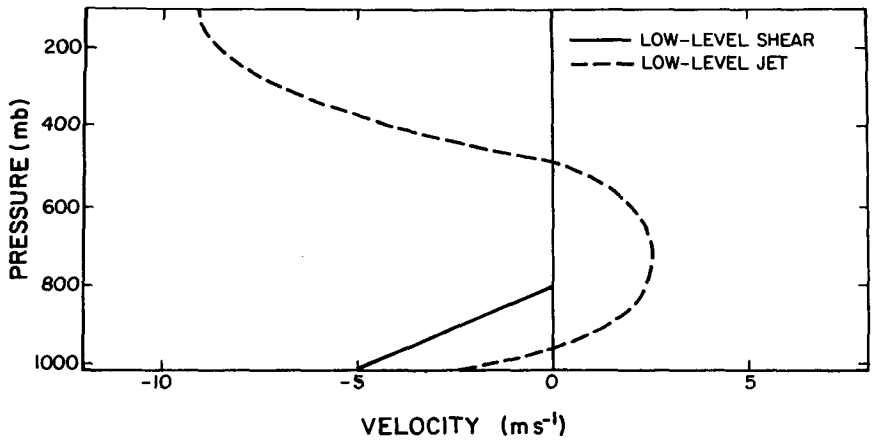

FIG. 3. Initial wind profiles for low-level shear and low-level jet cases.

after 1200 EST at the sea-breeze fronts. By 1400 EST weak deep convection occurs at the west coast sea-breeze front. Figures 4a,b,c, and d show fields of temperature perturbation, horizontal velocity, vertical velocity, and total liquid- and ice-water content, respectively, at 1500 EST (in this and subsequent figures the thick solid line at the surface, between $x = -100$ km and $x = 100$ km, represents the peninsula, the remaining region is the sea). The first grid level above the surface (200 m) has warmed by approximately 5K. The east coast sea breeze situated at $x = 30$ km has moved inland nearly twice as far as the west coast sea breeze situated at $x = -60$ km (Fig. 4b). The convection near the west coast has almost decayed and the deepest convection is now at the westward moving sea-breeze front. Although convection is deep, maximum vertical velocities are only ~ 3 m s^{-1}. Maximum liquid- and ice-water contents are ~ 2 g kg^{-1}.

Convergence of the westward and eastward moving sea-breeze fronts results in explosive development at 1600 EST. Figures 5a,b,c,d, and e show fields of horizontal velocity, vertical velocity, total liquid- and ice-water content, temperature perturbation and pressure perturbation, respectively, at 1700 EST. The updraft is tilted from the vertical as would be expected from the existence of environmental wind shear. Maximum vertical velocities in the updraft are ~ 8 m s^{-1} and it feeds on warm peninsula air coming from the east (Figs. 5a,d). The total liquid- and ice-water contents are high and spatially concentrated within a 25-km wide region over the west side of the peninsula. Compensating subsidence on either side of the updraft has led to midlevel warming and associated surface low pressure regions with high pressure perturbations aloft. Although warming through most of the troposphere is also large within the region of active convection, waterloading has a significant effect in reducing the surface pressure lowering in this area (Nicholls et al. 1988). An observational study by Cunning and DeMaria (1986) found extensive surface pressure lows forming beneath developing Florida convection, which is consistent with these modeling results. During the next hour there is a weakening in strength of the main updraft.

TABLE 1. List of experiments.

Experiment	Description
1	Type 1 wind profile
2	Type 2 wind profile
3	Type 3 wind profile
4	No wind
5	Low-level shear
6	Low-level jet
7	Moist midlevels Type 1 wind
8	Moist midlevels, Type 3 wind
9	Very moist midlevels, Type 3 wind
10	Modified boundary layer, Type 1 wind
11	More stable, Type 2 wind
12	More stable, dry midlevels, Type 2 wind
13	Moist soil, Type 1 wind
14	Dry soil, Type 1 wind
15	No microphysics, Type 1 wind

Figures 6a,b,c and d, show fields of vertical velocity, total liquid- and ice-water content, temperature perturbation and pressure perturbation, respectively, at 1800 EST. The vertical velocity has weakened considerably and there is a significant decrease in the total liquid- and ice-water content at upper levels and near the surface. This decay in system intensity produces two, deep gravity waves that propagate in opposite directions similar to the waves simulated by Tripoli and Cotton (1989a,b) for a decaying orogenic mesoscale convective system. The better-defined eastward moving wave is centered at $x = 60$ km. It is characterized by a deep, warm region with a positive pressure perturbation aloft and a negative pressure perturbation at low levels. This disturbance can be traced back to the perturbations induced by compensating subsidence shown in Figs. 5d,e, at 1700 EST. A more detailed look

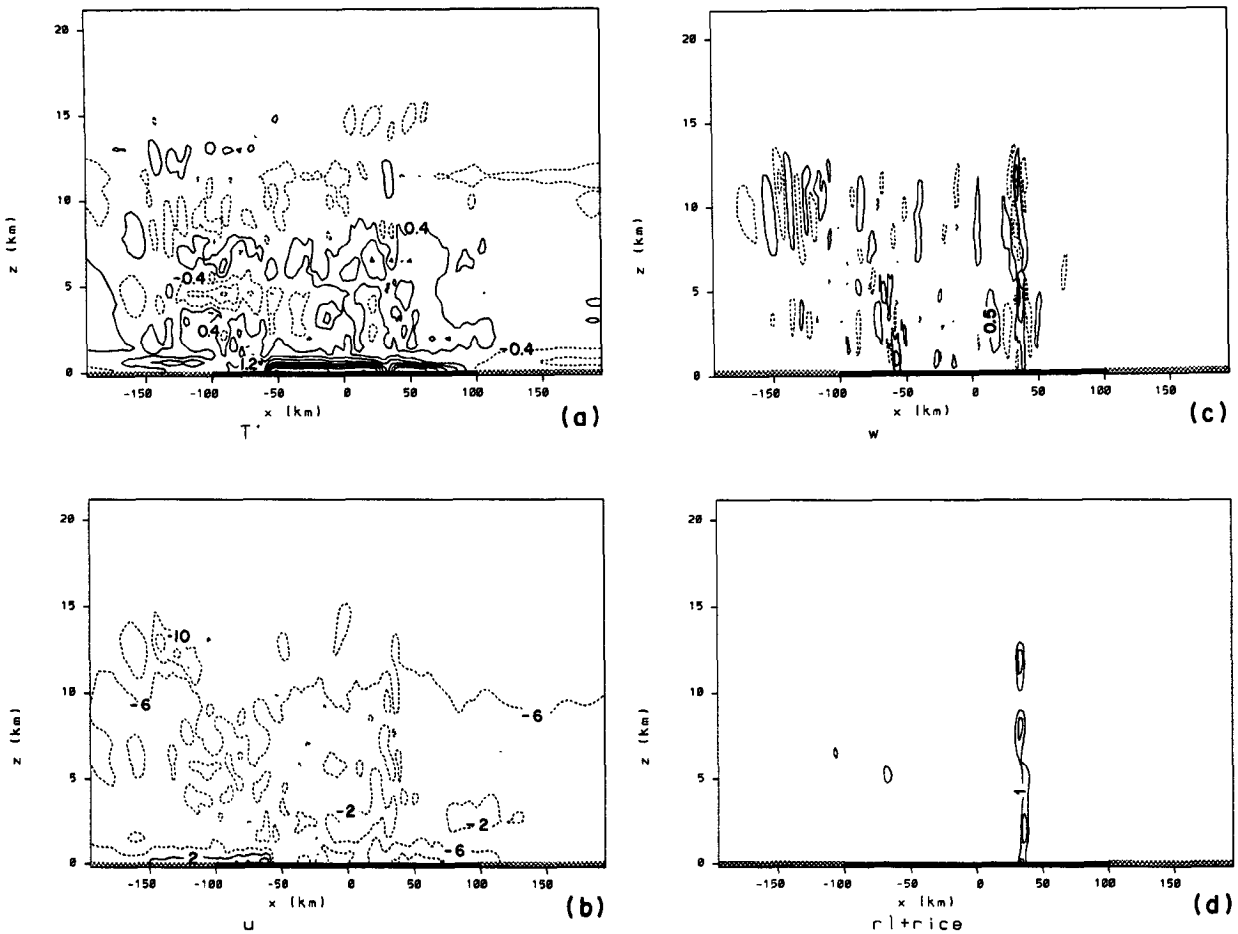

FIG. 4. Results for the Type 1 wind profile at 1500 EST (a) temperature perturbation from the initial state. The contour interval is 0.8°C. (b) Horizontal velocity (u component). The contour interval is 4 m s^{-1}. (c) Vertical velocity. The contour interval is 1 m s^{-1}. (d) Total liquid- and ice-water content. The contour interval is 1 g kg^{-1}. Negative isopleths are dashed and positive isopleths are solid.

at the velocity field (not shown) reveals that the disturbance is a clockwise rotating roll. Downward motion at the leading edge builds the disturbance by producing adiabatic warming and associated pressure perturbations, while upward motion at the back edge leads to diabatic cooling that erodes the disturbance. The weakening in intensity of the initial strong updraft appears to be due to the fallout of precipitation resulting in a downdraft circulation developing at low levels. Melting and evaporation of precipitation results in low-level cooling and new updrafts form on the leading edges of this spreading cold pool. Figures 7a,b show the temperature perturbation and pressure perturbation fields, respectively, at 1900 EST. The eastward moving wave is exiting the right side of the domain with only a slight weakening in intensity. The westward moving wave has already exited the left side of the domain. A simple linear analytic model of this type of wave will be presented in a future study, which shows the propagation velocity is given approximately by $c = NH/\pi$ where N is the Brunt–Väisälä frequency and H the depth of the disturbance. For $N = 10^{-2}$ s^{-1} and $H = 8$ km, $c \approx 25$ m s^{-1}, which agrees well with the speed of the simulated disturbance. The Rossby radius of deformation (Rossby 1938) is defined as $L = c/f$ where f is the Coriolis parameter. The Rossby radius for this deep mode is approximately 400 km, hence for this simulation the gravitational response dominates the inertial.

Also evident from the temperature perturbation field is that most of the warm peninsula air feeding the system from the east has been exhausted. Figures 8a,b show fields of vertical velocity and total liquid- and ice-water content at 2000 EST. The main convection is situated just off the west coast. There is little buoyant air left for the system to feed on and the updraft velocities have weakened considerably. Convection continues to weaken and move westward out over the ocean. By 2400 EST the remnants of convection are exiting the left side of the domain.

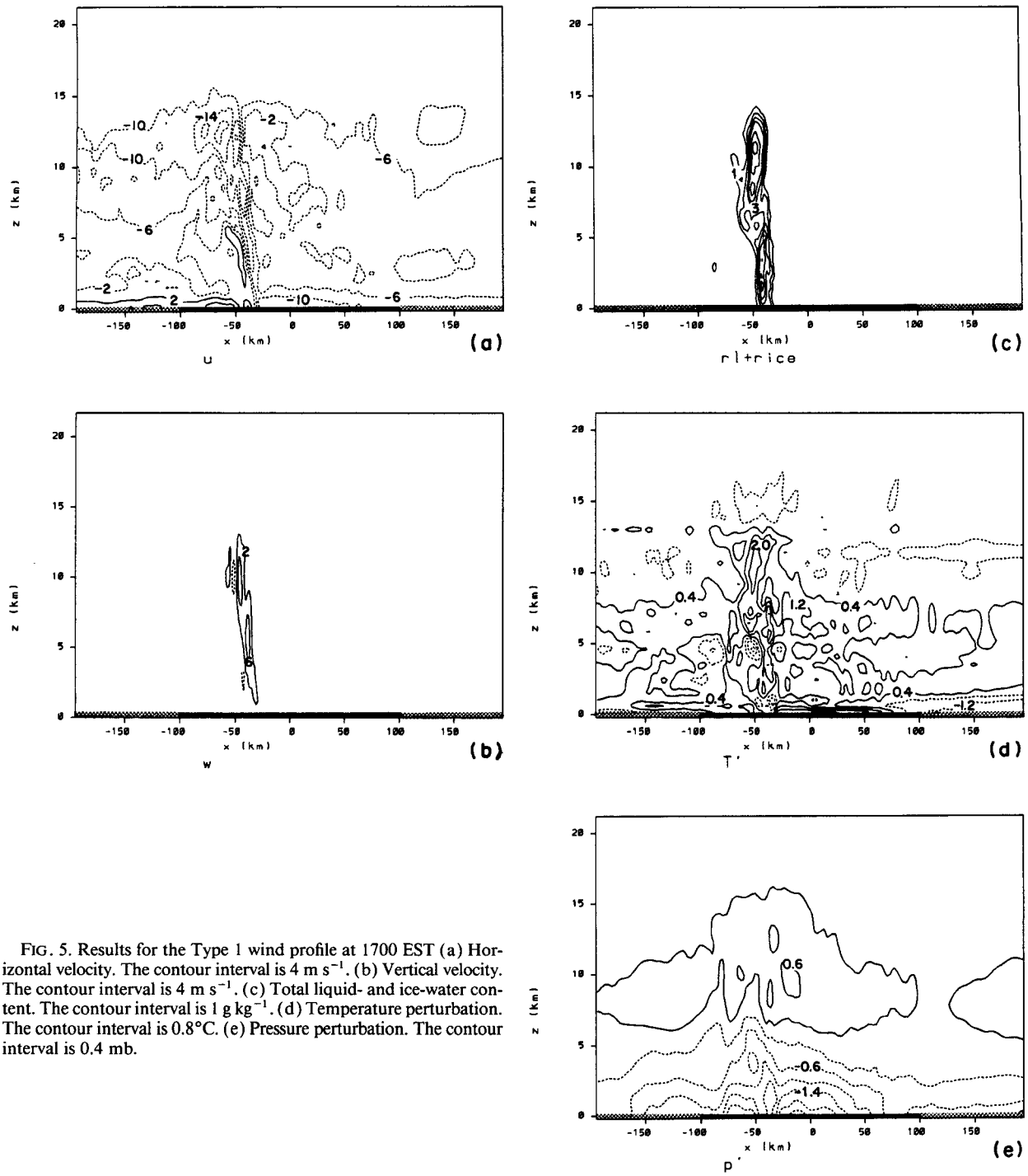

FIG. 5. Results for the Type 1 wind profile at 1700 EST (a) Horizontal velocity. The contour interval is 4 m s^{-1}. (b) Vertical velocity. The contour interval is 4 m s^{-1}. (c) Total liquid- and ice-water content. The contour interval is 1 g kg^{-1}. (d) Temperature perturbation. The contour interval is 0.8°C. (e) Pressure perturbation. The contour interval is 0.4 mb.

2) TYPE 2 WIND PROFILE

The thermodynamic sounding used in this experiment is shown by the solid line in Fig. 1 and the wind profile by the dashed line in Fig. 2. Development proceeds in a very similar manner to the Type 1 wind profile case. The east coast sea breeze moves inland faster, whereas the west coast sea breeze moves slower. Again, the first deep cell develops at the west coast sea-breeze front and this occurs just before 1500 EST. This initial deep cell is advected over the sea and decays. New deep cells subsequently develop at both sea-breeze

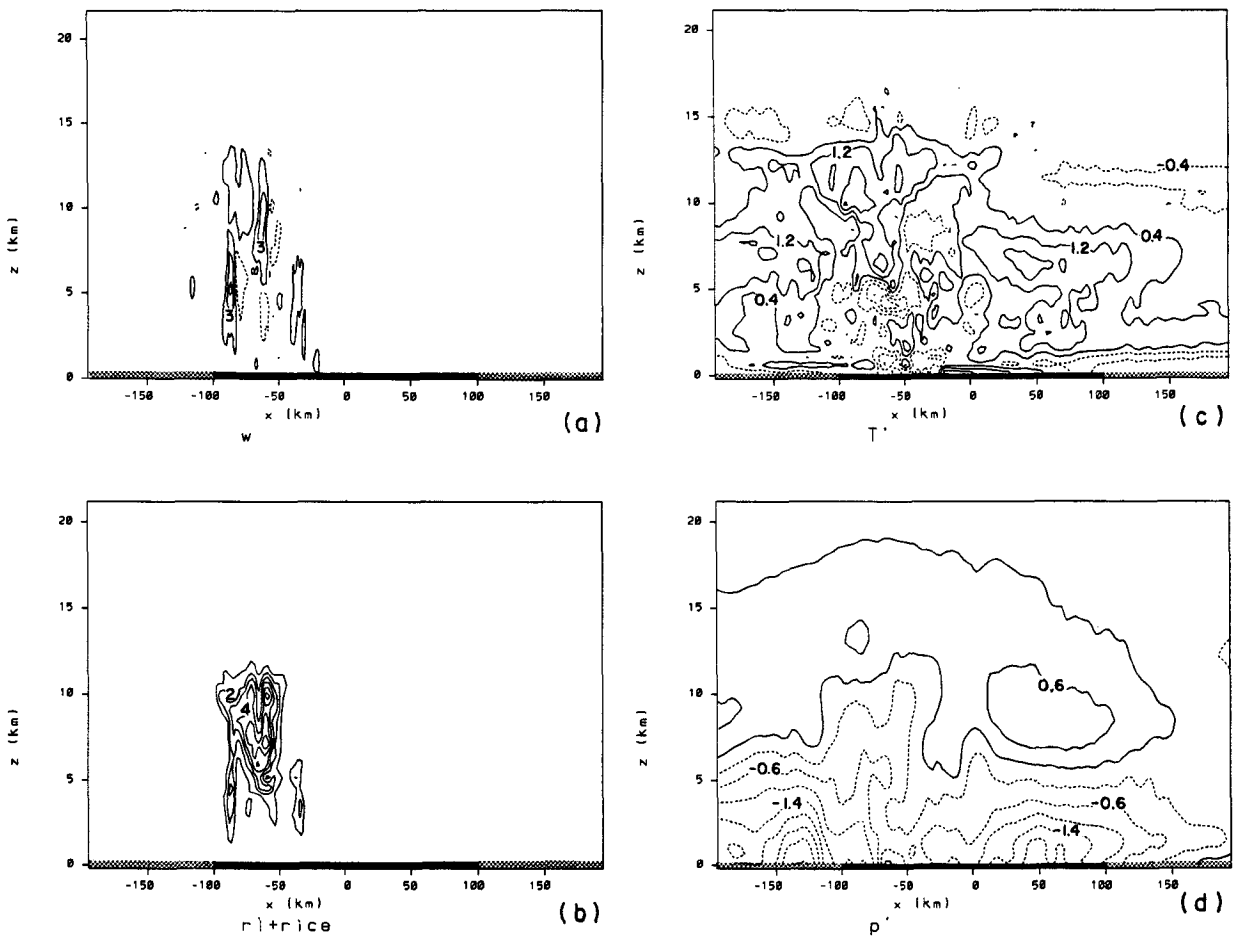

FIG. 6. Results for the Type 1 wind profile at 1800 EST (a) Vertical velocity. The contour interval is 2 m s^{-1}. (b) Total liquid- and ice-water content. The contour interval is 1 g kg^{-1}. (c) Temperature perturbation. The contour interval is 0.8°C. (d) Pressure perturbation. The contour interval is 0.4 mb.

fronts. The sea breezes converge at 1600 EST and at $x = -60$ km, which is about 20 km west of where convergence occurred for the Type 1 wind profile. At 1700 EST intense convection is located at $x = -75$ km. This cell moves over the sea and decays, but continual redevelopment of convection takes place just inland of the west coast. Figures 9a,b show fields of vertical velocity and total liquid- and ice-water content at 2000 EST. Convection is strongest just inland of the west coast. The remnants of an earlier cell can be seen advecting westward over the sea. Although the positioning and timing of convection agrees well with observations, the system was only slightly weaker than for the Type 1 wind profile case, whereas observations indicate Type 2 days are considerably weaker. The reason for this is probably that Type 2 days have less mid-level moisture than Type 1 days and lapse rates tend to be more stable. Sensitivity experiments to these variables are discussed later (experiments 11 and 12).

3) TYPE 3 WIND PROFILE

The thermodynamic sounding used in this experiment is shown by the solid line in Fig. 1 and the wind profile by the dotted line in Fig. 2. This case is in many ways a mirror image of the Type 1 wind profile simulation. However, there is slightly more shear below 600 mb and significantly stronger shear above 500 mb. Early on, convection is slightly stronger near the west coast. Rapid development begins at 1600 EST, located 10 km east of the center of the peninsula, whereas for the Type 1 wind profile case, convection occurs 35 km from the center. Figures 10a,b show fields of vertical velocity and total liquid- and ice-water content, respectively, at 1700 EST. Updraft velocities are strongest in the upper troposphere and the cloud top protrudes into the lower stratosphere. Figures 11a–c, show the vertical velocity, temperature perturbation and total liquid- and ice-water fields, respectively, at 1800 EST.

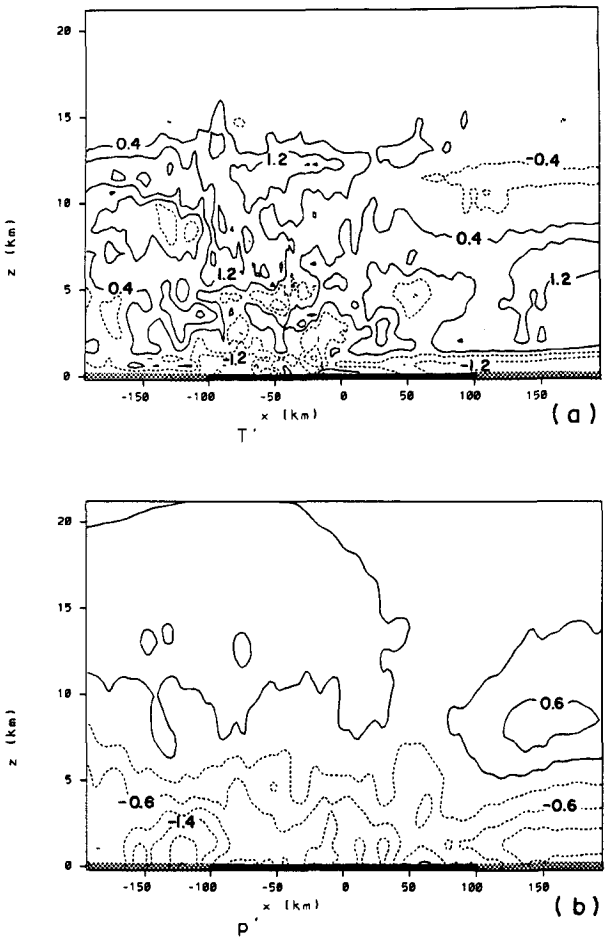

FIG. 7. Results for the Type 1 wind profile at 1900 EST (a) Temperature perturbation. The contour interval is 0.8°C. (b) Pressure perturbation. The contour interval is 0.4 mb.

Updraft strengths have weakened considerably. The warm low-level air over the peninsula has been replaced by rain cooled air. Two pronounced oppositely moving deep gravity waves were generated as the initially intense convection weakened. These can be seen in the temperature perturbation field, centered at $x = -150$ km and at the right lateral boundary. Quite strong warming exists just below the tropopause. In this region there is an extensive pristine ice crystal anvil, 2–3 km deep. Since the mixing ratios of these pristine ice crystals is small they are not evident in Fig. 11c. Most of the liquid and ice water has fallen to lower levels and some cooling can be seen at the melting level. Convection moves slowly eastward but never reaches the east coast and is very weak by 1900 EST.

The simulated convection does not last as long as observations indicate for Type 3 days. Increasing the midlevel moisture (experiments 8 and 9 discussed later) does not greatly affect the longevity of the cloud system, although it produces stronger convection earlier in the day in better agreement with observations. Blanchard and Lopez (1985) note that a 700-mb trough typically exists on Type 3 days and it is possible that synoptic-scale forcing is responsible for the longevity of the convection. Another apparent discrepancy with observations is that the east coast sea breeze moves inland instead of remaining stationary. The model results in this regard do not seem unreasonable considering that the westerly component of the wind is very weak at low levels (Fig. 2).

4) No wind

In this experiment, the thermodynamic sounding is shown by the solid lines in Fig. 1 and there is no initial wind. Fairly symmetrical sea-breeze circulations form early. However, symmetry is not perfect since small random temperature perturbations are introduced into the level nearest the surface initially. The influence of these random temperature perturbations on the re-

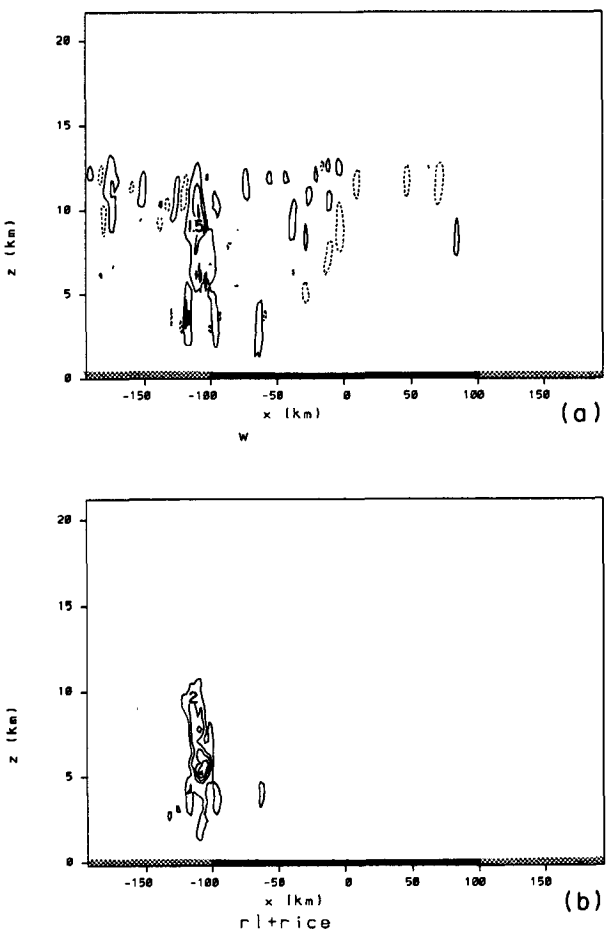

FIG. 8. Results for the Type 1 wind profile at 2000 EST (a) Vertical velocity. The contour interval is 1 m s^{-1}. (b) Total liquid- and ice-water content. The contour interval is 1 g kg^{-1}.

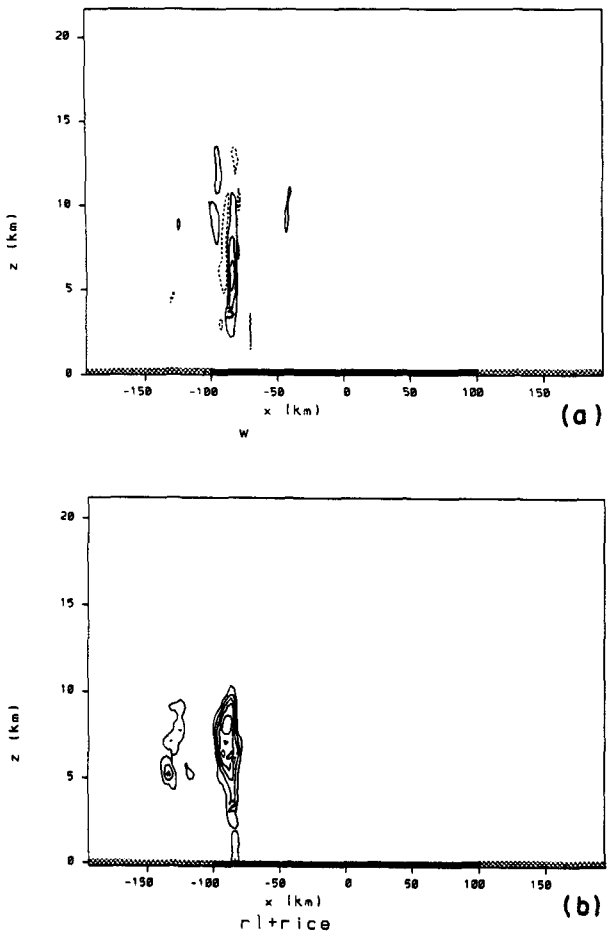

FIG. 9. Results for the Type 2 wind profile at 2000 EST (a) Vertical velocity. The contour interval is 2 m s^{-1}. (b) Total liquid- and ice-water content. The contour interval is 1 g kg^{-1}.

sulting simulations is discussed in section 5. By 1400 EST a weak deep cell forms on the east side of the peninsula, which has no counterpart on the west side. This first deep cell produces low-level cooling over the east side of the peninsula. At 1500 EST a quite intense cell develops in the warm air over the west side of the peninsula as the cell to the east decays. This cell in turn decays and at 1700 EST a new intense cell forms at the center of the peninsula which persists, although weakening in intensity, until the end of the simulation.

5) LOW-LEVEL SHEAR

The thermodynamic sounding used in this experiment is shown by the solid lines in Fig. 1 and the wind profile by the solid line in Fig. 3. Since there are easterly winds at low levels, the westward moving sea breeze moves rapidly inland. Deep convection occurs at both sea-breeze fronts at 1500 EST. The convection at the westward moving sea-breeze front, located at the center of the peninsula remains strong and persistent for the next two hours. It feeds on low-level warm air coming from the east. The persistence of this convection may be related to the low-level shear interacting with the cold pool formed by evaporational cooling as discussed by Rotunno et al. (1988). This convection at the center of the peninsula weakens at 1800 EST and a new vigorous cell forms 35 km to the west. This cell in turn starts to decay by 2000 EST and another fairly weak cell has formed 35 km to the west.

6) LOW-LEVEL JET

The thermodynamic sounding used in this experiment is shown by the solid lines in Fig. 1 and the wind profile by the dashed line in Fig. 3. Convection for this simulation is initially stronger on the west coast. Although the lowest-level winds are weak easterlies, the

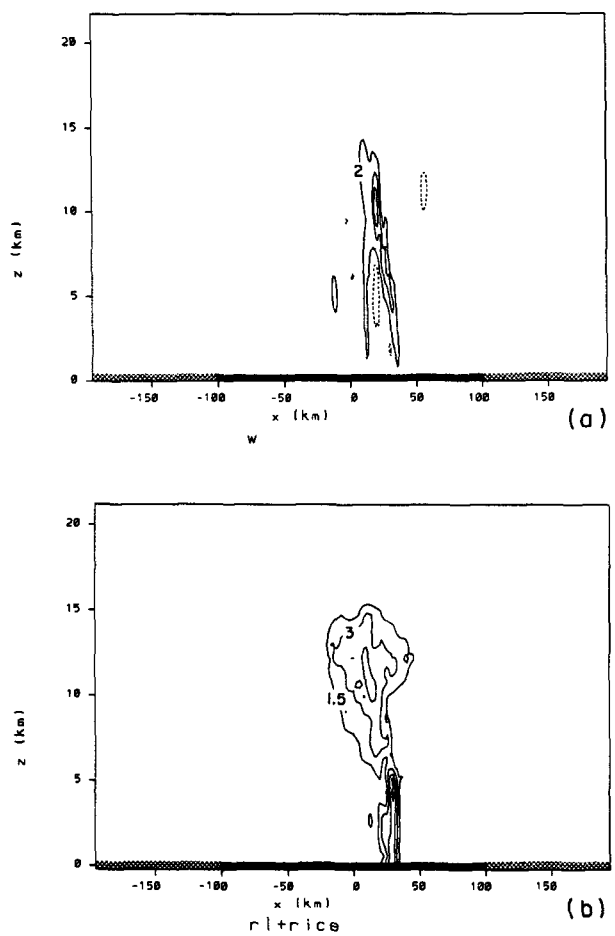

FIG. 10. Results for the Type 3 wind profile at 1700 EST (a) Vertical velocity. The contour interval is 4 m s^{-1}. (b) Total liquid- and ice-water content. The contour interval is 1.5 g kg^{-1}.

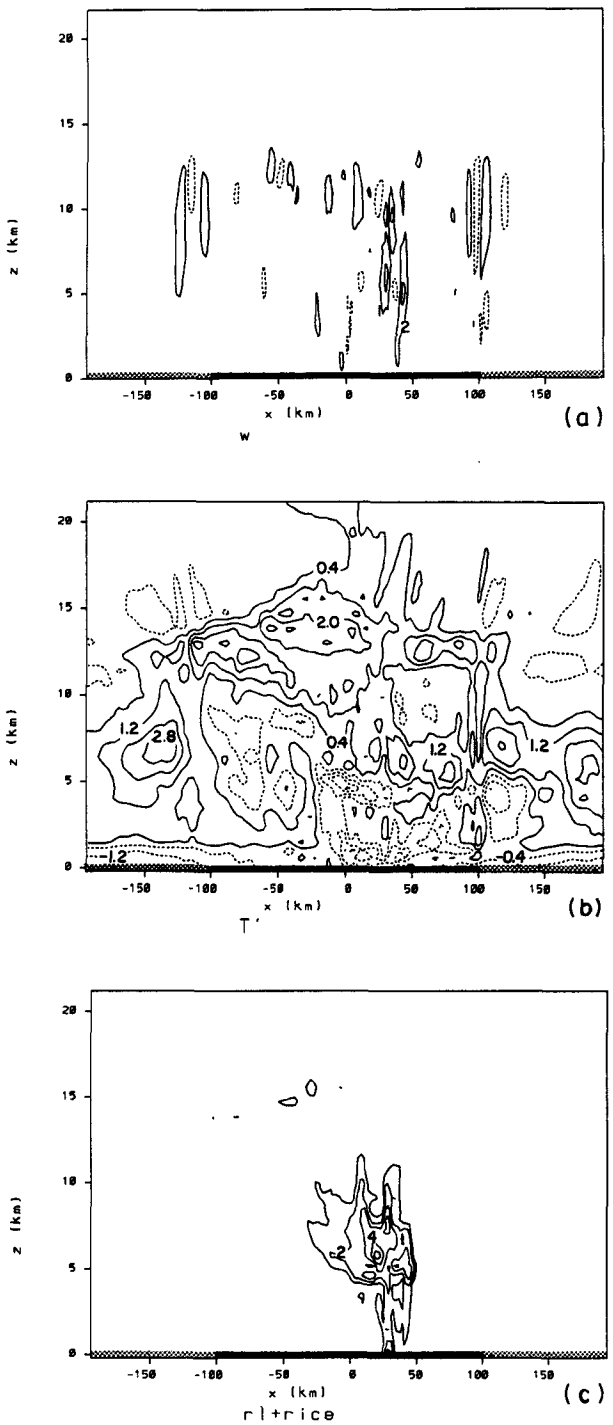

FIG. 11. Results for the Type 3 wind profile at 1800 EST (a) Vertical velocity. The contour interval is 2 m s^{-1}. (b) Temperature perturbation. The contour interval is 0.8°C. (c) Total liquid- and ice-water content. The contour interval is 1 g kg^{-1}.

surface cooling associated with the stronger convection on the west coast and the presence of westerlies above 1 km appears to cause the eastward moving convergence line to propagate inland as fast as the westward moving line. Rapid development begins at 1600 EST at the center of the peninsula. Convection moves slowly eastward and starts to form a trailing stratiform region. However, convection weakens and by 2000 EST only remnants remain 50 km from the center of the peninsula.

7) MOIST MIDLEVELS, TYPE 1 WIND

The temperature and dewpoint temperature profiles used in this experiment are shown by the solid and dashed lines, respectively, in Fig. 1, and the wind profile by the solid line in Fig. 2. Deep convection developed earlier for this case than for experiment 1 (Type 1 wind profile). At 1400 EST weak, deep convection occurs at both sea-breeze fronts. Deep convection at the sea-breeze fronts causes them to propagate inland faster, due to evaporational cooling and waterloading enhancing the pressure gradient across the front. This appears to account for the location of the convergence of the oppositely moving sea breezes being slightly to the west ($\sim$10 km) of where it was in experiment 1; since for experiment 1 early deep convection occurred only at the eastward moving sea-breeze front. Rapid development of convection as the sea-breeze fronts converge, occurs approximately 30 min earlier than in experiment 1, which is also consistent with the faster movement of the westward moving sea breeze. Another difference is that the updraft that forms when the sea breezes converge is more persistent. In contrast, in experiment 1, two distinct new updrafts form on both sides of the spreading cold pool as the initial updraft weakens. For this moister midlevel case, the initial updraft maintains itself as an entity feeding off low-level warm air coming from the east side of the peninsula. Nevertheless, it did weaken considerably after the initial rapid development and two well-defined oppositely moving deep gravity waves were produced.

8) MOIST MIDLEVELS, TYPE 3 WIND

The temperature and dewpoint profiles used in this experiment are shown by the solid and dashed lines, respectively, in Fig. 1, and the wind profile by the dotted line in Fig. 2. As in experiment 7 (moist midlevels, Type 1 wind profile) weak, deep convection develops at both sea-breeze fronts at about the same time. Intense convection occurs at 1600 EST, located 25 km east of the center of the peninsula. Convection moves eastward and decays 30 km from the east coast at 2000 EST. There is some building back of the convection towards the middle of the peninsula at 2000 EST. This case is similar to experiment 3 (Type 3 wind) except the increased midlevel moisture causes convection to be stronger, rapid development occurs slightly earlier, and the system decays further to the east.

9) VERY MOIST MIDLEVELS, TYPE 3 WIND

The temperature and dewpoint temperature profiles used in this experiment are shown by the solid and dotted lines, respectively, in Fig. 1, and the wind profile by the dotted line in Fig. 2. Deep convection develops early for this case (by 1300 EST) at both sea-breeze fronts, although it is strongest on the west coast. The west coast convection moves eastwards, merging with cells that developed in between the sea-breeze fronts. This convection subsequently decays and rapid growth of a new cell occurs at 1600 EST in the center of the peninsula. This convection moves eastward slightly faster than for the drier midlevel cases, which have the same wind profile (experiments 3 and 8) and decays closer to the east coast. The larger midlevel moisture content does not greatly affect the longevity of the system.

10) MODIFIED BOUNDARY LAYER, TYPE 1 WIND

The thermodynamic and wind profiles used in this experiment are shown by the solid lines in Figs. 1 and 2. Additionally, the surface temperature and moisture are increased by 2°C and 1 g kg^{-1}, respectively. These perturbations linearly decrease to zero at a height of 1 km. Convection develops early in this simulation (1130 EST) since the initial surface temperature is closer to the convective temperature. Figures 12a–c show the vertical velocity, temperature perturbation, and total liquid- and ice-water content, respectively, at 1500 EST. There is a fairly deep outer cell at $x = -70$ km and a weaker decaying outer cell at $x = 40$ km. In between, a more intense and deeper cell has developed. Significant modification of the warm, surface air over the peninsula has already occurred. This middle cell decays during the next hour. The deepest and most intense cell occurs at 1700 EST and is located at $x = -70$ km. This advects westward and decays over the west coast. A new cell begins to develop at 1900 EST, located at $x = -35$ km and is still quite strong at 2000 EST.

11) MORE STABLE, TYPE 2 WIND

The temperature and dewpoint temperature used in this experiment are shown by the dash–dot and solid line, respectively, in Fig. 1, and the wind profile by the dashed line in Fig. 2. The early cells that develop at the sea-breeze fronts are weak. At 1600 EST the sea-breeze fronts have still not converged, and each has produced two weak, deep cells located at $x = -10$ km and $x = -60$ km. By 1700 EST, the cell at $x = -60$ km has undergone rapid development and is moving westward, whereas the cell to the east at $x = -10$ km has decayed. The intense westward moving cell eventually decays over the sea at 1900 EST. A new cell develops slightly inland, and by 2000 EST has advected westward over the sea.

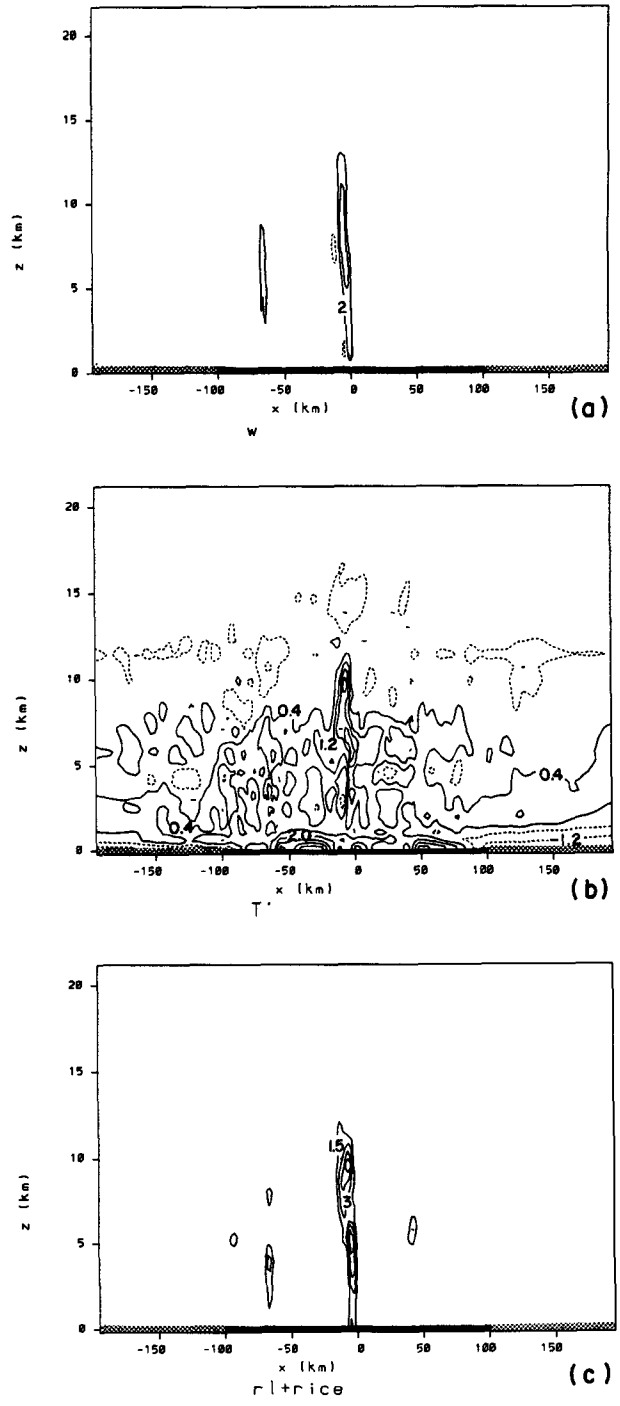

FIG. 12. Results for the modified boundary layer case (experiment 8) at 1500 EST (a) Vertical velocity. The contour interval is 4 m s^{-1}. (b) Temperature perturbation. The contour interval is 0.8°C. (c) Total liquid- and ice-water content. The contour interval is 1.5 g kg^{-1}.

12) More stable, dry midlevels, Type 2 wind

The temperature and dewpoint temperature profiles used in this experiment are shown by the dash–dot lines in Fig. 1, and the wind profile by the dashed line in Fig. 2. Similarly to experiment 11 (more stable, Type 2 wind), early convection is weak and the oppositely moving sea-breeze fronts have not converged by 1600 EST. Again two cells form at the sea-breeze fronts. However, in this case it is the cell at the westward moving sea-breeze front that develops rapidly at 1700 EST. As this cell moves with the mean midlevel winds it merges with a new cell that develops just to the west of it. At 2000 EST convection is located 20 km offshore.

13) Moist soil, Type 1 wind

The thermodynamic and wind profiles used in this experiment are shown by the solid lines in Figs. 1 and 2, respectively. The soil moisture content is increased to 80% of the maximum volumetric content. In this case the sea breezes initially move inland more slowly, since more of the solar heating is used to evaporate soil moisture, resulting in reduced sensible heat fluxes and less surface warming. By 1400 EST the first grid level above the surface (200 m) has only warmed up by 3K compared to 5K for experiment 1. Deep convection initially occurs at the westward moving sea-breeze front (note that for experiment 1 it occurred at the eastward moving front) at 1400 EST. No significant convection occurs at the eastward moving front until 1600 EST. Subsequently, this becomes the dominant cell with intense convection located at $x = -70$ km occurring at 1800 EST. This convection moves westward and decays over the coast. Some weak convection occurs just inland of the west coast at 2000 EST.

14) Dry soil, Type 1 wind

The thermodynamic and wind profiles used in this experiment are shown by the solid lines in Figs. 1 and 2, respectively. The soil moisture content is decreased to 10% of the maximum volumetric content. Figures 13a–c show fields of horizontal velocity, temperature perturbation, and total liquid- and ice-water content, respectively, at 1400 EST. The decrease in surface moisture produces stronger sensible heat fluxes that cause the sea breezes to move inland more quickly. The stronger convergence at the sea-breeze fronts appears to be responsible for quite deep convection early on at 1400 EST, at both fronts. The cell at the westward moving sea-breeze front at $x = 10$ km is considerably stronger than the cell at the eastward moving front at $x = -80$ km. However, by 1500 EST a new cell that forms at the eastward moving front, at $x = -50$ km, is more intense. These outer cells move westward eventually decaying and a new cell develops in between them, which by 1700 EST is quite intense and located at $x = -60$ km. This cell decays during the next hour and yet another cell develops further to the east at x

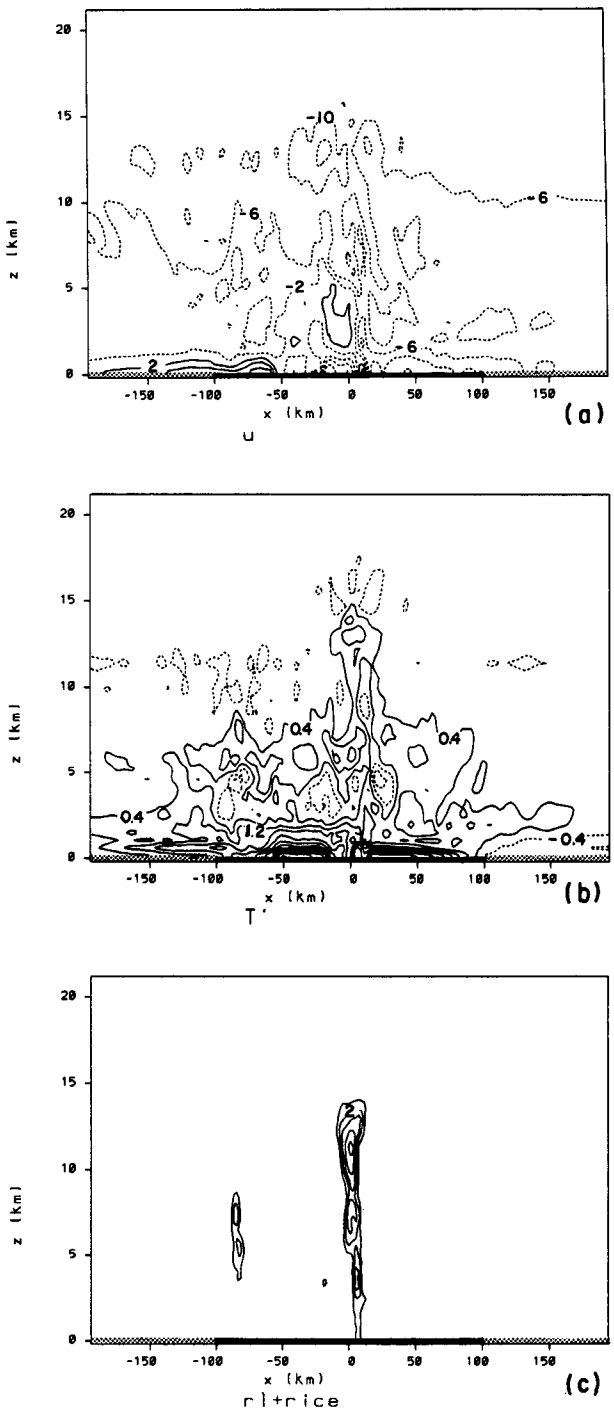

FIG. 13. Results for the dry soil case (experiment 10) at 1400 EST. (a) Horizontal velocity. The contour interval is 4 m s^{-1}. (b) Temperature perturbation. The contour interval is 0.8°C. (c) Total liquid- and ice-water content. The contour interval is 1 g kg^{-1}.

= −30 km. This cell moves westward and decays near the coast. A weak cell develops just off the west coast at 2000 EST.

15) NO MICROPHYSICS

This simulation is identical to experiment 1 except the microphysical parameterizations are not activated. Figures 14a,b show fields of vertical velocity and water-vapor perturbation, respectively, at 1400 EST. There is considerable small-scale cellular activity between the convergent sea breezes, which apparently develops due to Rayleigh–Bernard instability. The spacing between these cells is approximately 6 km. Figure 14b shows that these cells produce significant drying of the air near the surface and moistening above. These cells develop at 1200 EST and also occur in the simulations with microphysics, as will be discussed in the next section. The positions of the sea-breeze fronts for the simulation with microphysics (experiment 1) are 10 km further inland at 1400 EST. By 1600 EST the convergent sea-breeze fronts in this experiment are 75 km apart, with the midway point between them at $x = -30$ km. For the simulation with microphysics, rapid convective development at this time is situated at $x = -40$ km, which is close to the midway point. The depth of the cells has increased by ~0.5 km from values two hours earlier.

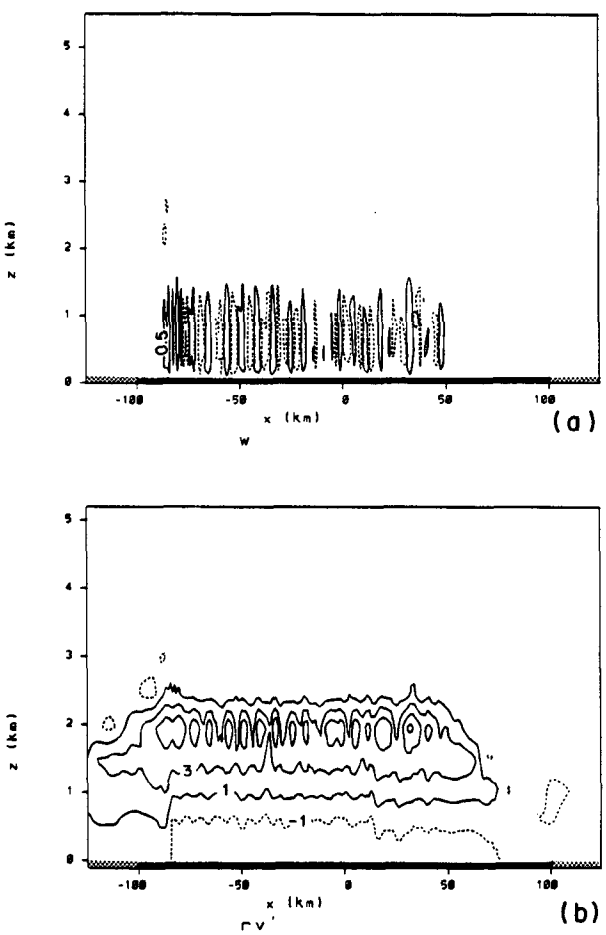

FIG. 14. Results for the no microphysics case (experiment 15) at 1400 EST (a) Vertical velocity. The contour interval is 1 m s^{-1}. The −0.5 m s^{-1} and +0.5 m s^{-1} contours are shown. (b) Water-vapor perturbation. The contour interval is 1 g kg^{-1}.

b. General properties

1) EARLY STAGES OF CONVECTIVE DEVELOPMENT

Early on in the simulations ($t < 1200$ EST) low-level warming and moistening occur due to surface fluxes. At ~1200 EST small-scale cells develop between the two converging sea-breeze fronts. Some of these cells appear to originate as waves forced at the sea-breeze fronts, especially when the low-level ambient wind opposes the motion of a front. Vertical motions associated with these cells are ~1 m s^{-1} and produce shallow clouds for the simulations with microphysics. Figures 15a,b show the simulated cloud-water field at 1300 EST for the moist soil case and the observed satellite visible images over Florida at 1300 EST 11 July 1989, respectively. The strongest convection in the simulation occurs at the leading edge of the sea-breeze fronts with shallow clouds in between, and this is in general agreement with observations. For the simulations with microphysics, these cells result in a moistening of ~1 g kg^{-1} between 1–3 km above the surface and drying of ~2 g kg^{-1} in the lowest kilometer compared to values an hour earlier. The cells in between the convergent sea-breeze fronts start to become fairly deep. However, the outer cells at the sea-breeze fronts grow more rapidly, and by approximately 1400 EST compensating subsidence appears to have suppressed the cells in between. For some simulations only one of the outer cells becomes deep, whereas for other simulations both outer cells develop. These first deep cells that develop are usually left behind by the more rapidly moving sea-breeze fronts. By 1500 EST one or two deep cells develop in between the converging sea-breeze fronts. Typically, during the next hour, one of these cells develops explosively while the other cells decay. Occasionally, this explosively developing cell merged with one of the outer cells, or one of the outer cells developed into the dominant region of convection.

Balaji and Clark (1988) propose a mechanism for the upscale development of convection in the absence of any strong forcing mechanism. The opportune phasing of gravity wave motions aloft with shallow convective clouds was shown to be capable of eventually leading to the development of deep convection. Clark et al. (1986) found that a strong shear layer in the region spanning the upper portions of the boundary layer and overlying stable layer appeared to define the

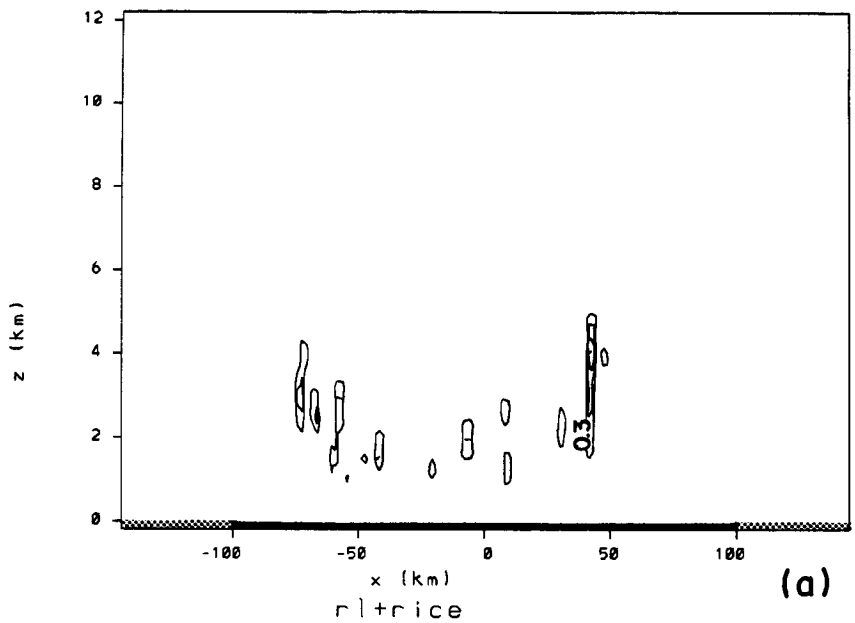

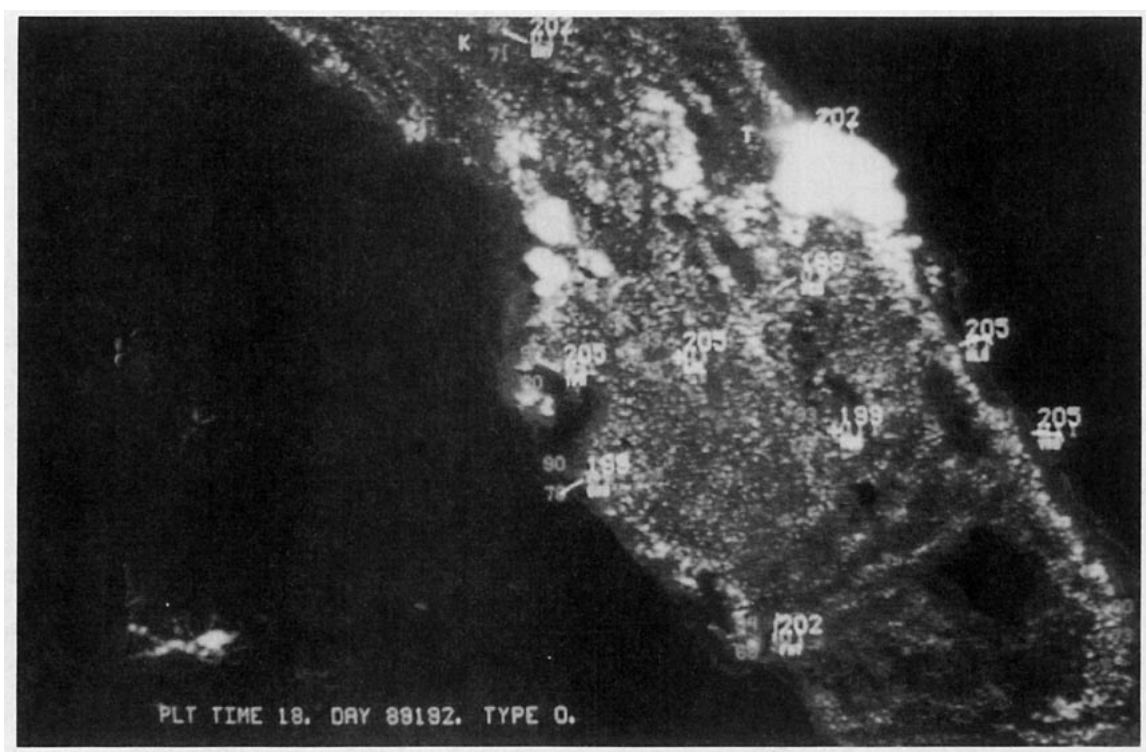

FIG. 15. (a) Simulated cloud-water field for the moist soil case at 1300 EST. The contour interval is 0.3 g kg^{-1}. (b) Satellite visible images over Florida at 1300 EST 11 July 1989, from GOES. Standard observations are plotted.

most favorable situation for the excitation of gravity waves. Strong shear was absent for the simulations in this study and no significant gravity wave activity occurred above the boundary layer prior to the development of cumulonimbus clouds. Furthermore, the stage during which shallow clouds existed in between the convergent sea breezes was short lived since they were suppressed as the outer cells developed. The low-level convergence of the oppositely moving sea breezes seems to be the most dominant control for determining

the timing and location of the strongest convective development. As the sea-breeze fronts converge the region of peninsula air having large convective available potential energy (CAPE) becomes more and more confined. CAPE accumulates in vertical columns during the earlier part of the day due to surface fluxes of heat and moisture. It is possible that the deep outer cells that develop at the sea-breeze fronts and that suppress convection between them play a role in allowing this buildup to occur. Typically, deep convection begins within this unsullied air when the oppositely moving sea-breeze fronts become within a few tens of kilometers of one another. By this time the low-level convergence associated with the sea-breeze circulations is of quite a large scale and this provides a sustained low-level forcing resulting in an intense cell developing at the center of convergence.

2) RAINWATER CONTENT AND PRECIPITATION

Total rainwater content gives an indication of the intensity of convection and the rainfall rate. Time series of total rainwater contents for the simulations with microphysics are shown in Fig. 16. Results for the Type 1 wind profile (Fig. 16a) shows rainwater forms just after 1200 EST. A rapid increase in rainwater content begins just before 1600 EST. This corresponds to the convergence of the oppositely moving sea breezes. A peak in rainwater content occurs at 1715 EST followed by a decline and then a stronger peak at 1845 EST. The decline in rainwater content after the first peak occurs as the initial updraft formed by the convergence of the oppositely moving sea breezes, weakens. The secondary peak occurs as new updrafts form on either side of the spreading cold pool. The Type 2 wind profile (Fig. 16b) also produces a fairly sharp increase in rainwater content as the sea breezes converge, just after 1600 EST, with a stronger secondary peak occurring at 1830 EST. Results for the Type 3 wind profile (Fig. 16c) show a more rapid increase in rainwater content at 1600 EST and the secondary peak is considerably weaker. For this case, convection has almost completely decayed by 2000 EST.

The no wind case (Fig. 16d) shows an early peak in rainwater content at 1500 EST, due to the cell that forms over the western side of the peninsula. Subsequently rainwater reaches a peak at 1730 EST and then declines. The rainwater for the low-level shear case is shown in Fig. 16e. Unlike the other experiments discussed so far, this case does not produce a strong maximum followed by a decline, and rainwater is still high at 2000 EST. The low-level jet case (Fig. 16f) is similar to the Types 1, 2, and 3 simulations in that a rapid increase in total rainfall occurs at 1600 EST; there is a secondary peak and a substantial decline by 2000 EST.

The moister midlevel simulations (Figs. 16g–i) produce considerably more net rainwater than the experiments already discussed. The moist midlevel, Type 1 wind case, shows a much stronger primary peak than experiment 1 (Type 1 wind, Fig. 16a), and this peak occurs 30 min earlier. The primary peak for the moist midlevel, Type 3 wind case also occurs slightly earlier than for experiment 3 (Type 3 wind, Fig. 16c). The very moist midlevels, Type 3 wind simulation produces high total rainwater in the early afternoon with the strongest peak occurring considerably earlier than for experiment 3 (Type 3 wind, Fig. 16c).

The modified boundary layer, Type 1 wind case (Fig. 16j) forms rainwater earlier than the experiments discussed so far, but magnitudes remain small until 1430 EST when an intense cell develops near the center of the peninsula. The most intense cell in this simulation begins at 1700 EST leading to the second peak in rainwater at this time. The rainwater remains high at 2000 EST, which is consistent with the initial environment having a warmer and moister boundary layer than for the other cases. The more stable, Type 2 wind case (Fig. 16k) produces rainwater later than the experiments already discussed. A rapid increase in rainwater begins at 1600 EST leading to a peak an hour later. At 2000 EST rainwater is still quite high. The more stable, dry midlevels, Type 2 wind simulation (Fig. 16l) produces rainwater even later than for the previous experiment. The peak in rainwater content does not occur until 1800 EST.

The moist soil, Type 1 wind simulation (Fig. 16m) forms rainwater later than for most of the other simulations. The largest rainwater also occurs late. In contrast, the dry soil Type 1 wind simulation (Fig. 16n) forms rainwater much earlier and the peak magnitude also occurs sooner.

Burpee and Lahiff (1984) found in their study that the area-averaged rainfall on sea-breeze days over south Florida showed a maximum at 1600 EST (Fig. 3 in their paper), whereas the maximum rainwater content for most of the simulations in this study occurs after 1600 EST. A possible reason for this discrepancy is that the averaging region they consider includes the southern-most portion of the peninsula, which is narrower than the 200-km cross section used in this study. A narrower land surface would lead to an earlier convergence of the oppositely moving sea breezes. This is supported by the observational study by Schwartz and Bosart (1979) who found that the rainfall maximum that occurs between 1600–1700 EST in the central, wider part of the peninsula occurs earlier further to the south (see Fig. 7 of their paper). Results of the present simulations also show a sensitivity of the timing of intense convection to soil moisture content and midlevel moisture. The trend found in these experiments that moist conditions at midlevels generally lead to the earlier development of intense convection is consistent with Burpee and Lahiff's observations of rainfall (see Fig. 5 of their paper). An aspect of the model pertinent to the timing of the onset of deep convection is the

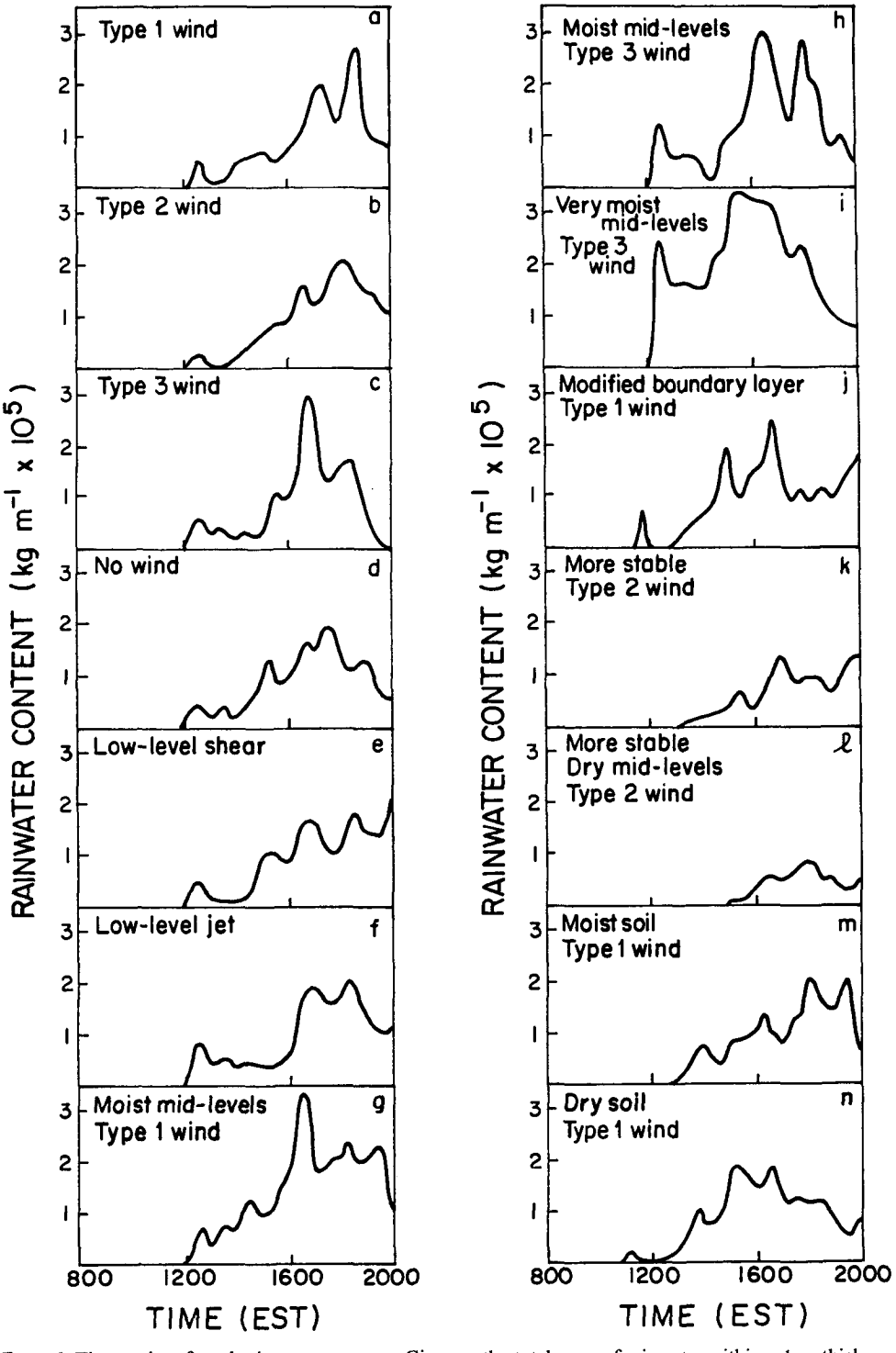

FIG. 16. Time series of total rainwater contents. Given as the total mass of rainwater within a 1-m thick section (400 km × 22 km × 1 m). Experiments are ordered from 1 to 14 and labeled a to n, respectively.

procedure for calculating the surface fluxes. For instance, the top of the surface layer is assumed to be at 200 m—the height above the surface of the lowest model grid point—even though surface-layer theory is only strictly applicable for the first few tens of meters. The sensitivity to the vertical resolution was tested to a certain degree by rerunning experiment 15 (no microphysics) but with twice the number of vertical grid

points, thereby placing the first theta level at 100 m above the surface. There were no significant differences between this run and the original simulation. Since the sea-breeze circulation is sensitive to surface heat fluxes, their accurate determination is of considerable importance, and there is clearly a need for further refinement and testing of the soil and surface layer parameterizations.

Figure 17 shows the accumulated precipitation reaching the surface between 0800 and 2000 EST for each point along the x axis. The Type 1 wind profile case (Fig. 17a) produces precipitation predominantly over the west side of the peninsula with a large peak at $x = -60$ km. The Type 2 wind profile case (Fig. 17b) peaks closer to the west coast at $x = -80$ km, whereas the Type 3 wind profile (Fig. 17c) produces precipitation over the east side of the peninsula with a large peak at $x = 25$ km. These results are in general agreement with the results of Blanchard and López (1985) for Types 1, 2, and 3 days, except less precipitation would be expected for Type 2 days, and Type 3 days tend to produce significant precipitation closer to the east coast.

The no-wind simulation (Fig. 17d) shows precipitation skewed to the west side of the peninsula. This is because of the strong cell that formed at 1500 EST on the west side of the peninsula. The low-level shear case (Fig. 17e) shows a peak rainfall accumulation at the center of the peninsula due to the persistent cell that formed there at 1500 EST. Peaks corresponding to the two other cells that formed successively 35 and 70 km to the west of this first intense cell are also apparent. The low-level jet case (Fig. 17f) is quite similar to experiment 3 (Type 3 wind, Fig. 17c) except the peak occurs slightly closer to the center of the peninsula.

The moist midlevels, Type 1 wind case (Fig. 17g) is similar to experiment 1 (Type 1 wind, Fig. 17a), except the magnitude of the peak accumulated precipitation is larger and forms slightly further to the west. The moist midlevels, Type 3 wind case (Fig. 17h) is similar to experiment 3 (Type 3 wind, Fig. 17c). The main difference is that more rainfall occurs farther to the east. The very moist midlevels, Type 3 wind simulation (Fig. 17i) does not produce such a pronounced single peak as occurs for the previous experiment or for experiment 3 (Type 3 wind, Fig. 17c), with the rainfall being more extensive. Significant rainfall now occurs near the east coast.

The modified boundary layer, Type 1 wind case (Fig. 17j) produces precipitation predominantly over the west side of the peninsula. Surprisingly, the increased environmental low-level temperature and moisture does not result in a very strong peak when compared to the other simulations. This may be because the land temperature is limited by the convective temperature. For this case, only a weak temperature contrast can develop resulting in a weaker sea-breeze circulation. The more stable, Type 2 wind simulation (Fig. 17k) produces less accumulated precipitation than the cases already discussed, with the maximum occurring near the west coast. Results for the more stable, dry midlevels, Type 2 wind case (Fig. 17l) shows very small accumulated precipitation amounts. The peak rainfall occurs farther towards the center of the peninsula than might be expected for the Type 2 wind profile. This is a consequence of the strongest cell developing on the westward moving sea-breeze front.

The moist soil, Type 1 wind case (Fig. 17m) produces a peak in precipitation to the east of the center of the peninsula due to a cell that formed on the westward moving sea-breeze front. The main precipitation occurred later near the west coast. The dry soil, Type 1 wind case (Fig. 17n) also formed a fairly strong cell at the westward moving sea-breeze front, causing a peak in the rainfall accumulation near the center of the peninsula. Most of the precipitation occurred later over the west side of the peninsula.

The peak values of the accumulated precipitation produced by the simulations often exceed 100 mm. An observational study by Ulanski and Garstang (1978) found that on one of the days they investigated (16 June 1973), the maximum point rainfall was greater than 100 mm. However, this occurred only in a small region of the FACE mesonetwork (an approximately 50 × 50 km square region just south of Lake Okeechobee) and the storm on this day was one of the most intense convective events during the 1973 experiment period. Cooper et al. (1982) calculated the average 15-min total rainfall amounts occurring in the FACE 1975 network for 47 wet and shower days in July–August (Fig. 15 of their paper). For a 4-h period beginning just before 1400 EST, the average rainfall rate was approximately 15 mm $(15\ \text{min})^{-1}$. Hence, the total rainfall over this 4-h period is considerably more than obtained for the simulations in this numerical study. However, they did not classify results into sea-breeze and synoptically disturbed days. Consequently, these high rainfall rates could be a result of synoptically disturbed conditions.

Table 2 shows the peninsula-averaged rainfall over the land surface for each of the experiments. This is calculated by summing the total rainfall occurring at each grid point over land during the 12-h simulation period and dividing by the number of grid points. This is a fairly good approximation to the daily rainfall, although some of the simulations still had active convection over land at 2000 EST (experiments 5 and 10, in particular). Burpee and Lahiff (1984) found the average rainfall for their observations of sea-breeze days during June–September to be 5.5 mm day^{-1}, and the maximum to be 14.5 mm day^{-1}. The majority of the numerical experiments produced average rainfall accumulations in excess of the maximum value of their observational study. The moister midlevel cases were particularly high. Nicholls and Weissbluth (1988) found for simulations of a tropical squall line that the

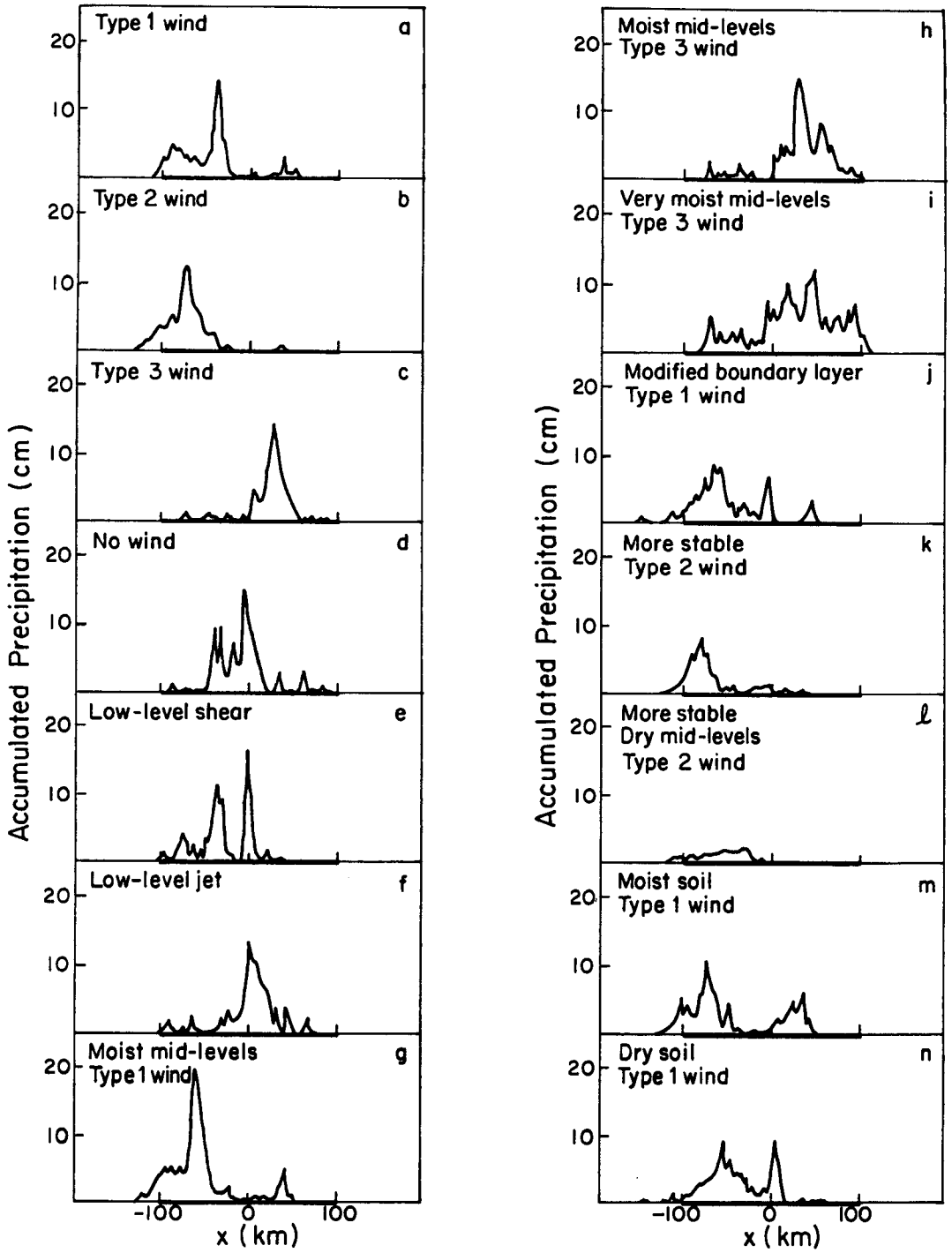

FIG. 17. Time-integrated rainfall as function of x. Experiments are ordered from 1 to 14 and labeled a to n, respectively.

precipitation produced in a three-dimensional model was ~75% of that in a two-dimensional model. If this carries over to Florida convection it would put the precipitation amounts for most of the experiments at the upper end of the observations made by Burpee and Lahiff. Since the 17 July 1973 was a heavy rain day (Cooper 1981), the simulated precipitation amounts do not appear that unreasonable. Clearly there is a need for three-dimensional simulations of Florida convection, which should be compared with detailed observational studies to determine how well the model can reproduce precipitation patterns and amounts.

TABLE 2. Peninsula-averaged rainfall.

Experiment	Description	Peninsula-averaged rainfall (mm)
1	Type 1 wind	16.5
2	Type 2 wind	16.1
3	Type 3 wind	17.5
4	No wind	19.5
5	Low-level shear	18.4
6	Low-level jet	19.2
7	Moist midlevels, Type 1 wind	24.8
8	Moist midlevels, Type 3 wind	26.7
9	Very moist midlevels, Type 3 wind	39.7
10	Modified boundary layer, Type 1 wind	18.9
11	More stable, Type 2 wind	10.7
12	More stable, dry midlevels, Type 2 wind	5.5
13	Moist soil, Type 1 wind	16.8
14	Dry soil, Type 1 wind	19.8

As mentioned in section 3, moist midlevel experiments (dashed line, Fig. 1) were not only carried out for the Type 1 and 3 wind profiles, but also for the Type 2 wind profile, no wind, low-level shear, low-level jet, modified boundary layer, moist soil, and dry soil cases. The moist midlevel experiments produced peak rainwater contents on average ~40 min earlier than for the control midlevel moisture cases. There was a tendency for deep convection to develop by 1400 EST at both sea-breeze fronts. This led to faster movement of the sea breezes causing the time at which convergence occurred to be slightly earlier. The stronger low-level convergence and the moister midlevel environment tended to produce a more rapid development of intense convection. Peninsula-averaged rainfall was higher than Burpee and Lahiff's results for sea-breeze days and more like some of the highly disturbed convective days they observed. For the no wind and low-level shear cases, early deep cells developed in the same manner as for the control midlevel moisture experiments. However, these early convective cells did not have such a significant influence on the precipitation pattern, with a greater proportion of the rainfall occurring later. Convection for the low-level shear simulation had significantly decayed by 2000 EST, unlike the control midlevel moisture case.

3) LARGE-SCALE HEAT AND MOISTURE BUDGETS

Neglecting subgrid-scale diffusion and horizontal eddy flux terms, the apparent heat source and moisture sink are given by

$$Q1 = \bar{Q} - \frac{\pi}{\rho_o}\frac{\partial}{\partial z}(\rho_o \overline{w'\theta'}), \quad (1)$$

$$Q2 = -L\left[\bar{e} - \bar{c} - \frac{1}{\rho_o}\frac{\partial}{\partial z}(\rho_o \overline{w'r_v'})\right], \quad (2)$$

where $\bar{Q}$ is the heating rate, e the evaporation rate, c the condensation, $\pi = c_pT/\theta$, ρ_o a base-state density; and other variables have their usual meaning. The overbar denotes a horizontal average over the domain and primes a perturbation from this average. Here, $Q1$ and $Q2$ represent the effects of convection on the large-scale variables as discussed by Yanai et al. (1973).

Results are shown for the apparent heat source, $Q1/c_p$ (°C day^{-1}), and the apparent moisture source, $-Q2/L$ (g kg^{-1} day^{-1}), in Figs. 18a,b, respectively, for various times and for experiment 1 (Type 1 wind profile). At 1000 EST the $Q1$ budget is positive beneath 1 km and slightly negative between 1–2 km. The warming is a consequence of the strong surface-sensible heat flux over the peninsula. The negative values above are due to longwave radiational cooling of the warm, moist air near the surface. The apparent moisture source is positive at low levels due to surface moisture fluxes. At 1200 EST, cells start to develop that cause heat to be transported vertically more efficiently. At the same time this results in a low-level drying and moistening above. As deep convection develops, $Q1$ starts to become large and positive. At 1500 EST the maximum in $Q1$ is at 4 km but by 1700 EST it has moved upward to 6.5 km (Fig. 18a). Some slight cooling occurs near the surface due to evaporational cooling. The apparent moisture source at 1700 EST is large and negative at low levels. Typically, the eddy fluxes of heat are comparatively small and the $Q1$ profile is similar to that of the latent heating. The main effect of the eddy fluxes of heat is to shift the maxima to slightly higher levels.

The eddy flux term is more significant for the apparent moisture source budget. The eddy moisture flux convergence is large at midlevels and opposes the drying effect due to condensation. At lower levels it contributes to large-scale drying. This has the effect of shifting the drying peak to significantly lower levels. These results are consistent with those of Lafore et al. (1988) for a simulation of a tropical squall line. Although, the apparent moisture source is negative at midlevels, the local rate of change of the mean vapor mixing ratio is slightly positive. This mean local midlevel moistening is opposed by large-scale vertical advection of moisture, resulting in a negative apparent moisture source. By 1900 EST the magnitude of the apparent heat and moisture sources are reduced; although the shape of the profiles are very similar to that two hours earlier. As convection decays later in the evening, $Q1$ is weak and positive above 5.5 km and weak and negative beneath. The apparent moisture source is still slightly negative at upper levels but very small at lower levels.

Observational analyses of $Q1$ and $Q2$ budgets over north Florida were made by Johnson (1976). The $Q1$ profile is similar to that obtained in this study, except that the small net cooling near the surface, due to rainfall evaporation, was not observed. The $Q2$ profile is also similar and shows a double-peak structure. However, the minimum found by Johnson occurs at 600 mb (by minimum is meant the weaker, large-scale

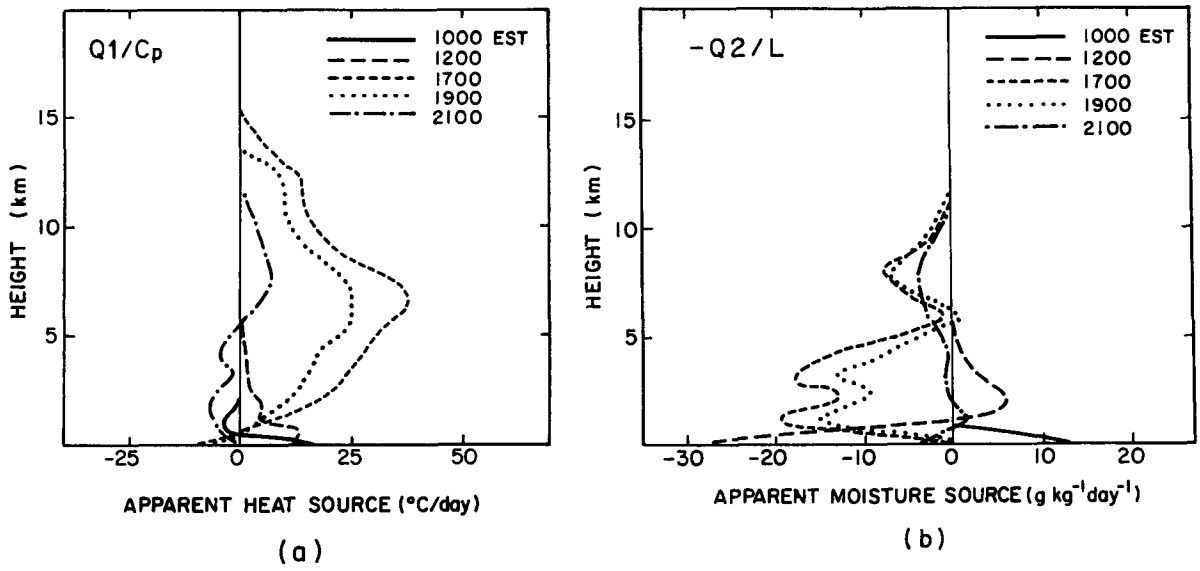

FIG. 18. (a) Apparent heat source budget. (b) Apparent moisture source budget.

drying region between the two peaks), whereas in this study it is higher, at 500 mb. Since the observations were made over north Florida during the passage of a weak tropical depression, this is probably not a significant discrepancy. The minimum for this simulation is a consequence of strong vertical convergence of the eddy moisture fluxes at this level. A similar result for a tropical squall line simulation was obtained by Lafore et al. (1988).

4) RADIATIONAL HEATING

Early on in the simulations, longwave radiational cooling of warm air near the surface occurs with a magnitude of $\sim 5°C\ day^{-1}$. At 1400 EST the deep clouds that develop at the sea-breeze fronts absorb shortwave radiation through most of their depth and this exceeds the longwave cooling by the clouds. Figures 19a,b show the shortwave and longwave radiational heating, respectively, at 1700 EST for experiment 3 (Type 3 wind profile case). Shortwave heating is confined to the top of the cloud that protrudes into the lower stratosphere. The magnitude is $\sim 10°C\ day^{-1}$ and extends through ~ 2 km depth. This heating is due to absorption by low mixing ratio, pristine ice crystals (these are not evident in the total liquid- and ice-water field shown in Fig. 10b due to the comparatively large contour interval used). Longwave radiational cooling is occurring at the top of the cloud and warming around the edges of the cloud at upper levels. This longwave cooling cancels the shortwave warming at cloud top. The net warming, at this time, is concentrated at the edges of the cloud at upper levels. An hour earlier, at 1600 EST, the shortwave warming was larger than the longwave cooling leading to a net warming at cloud

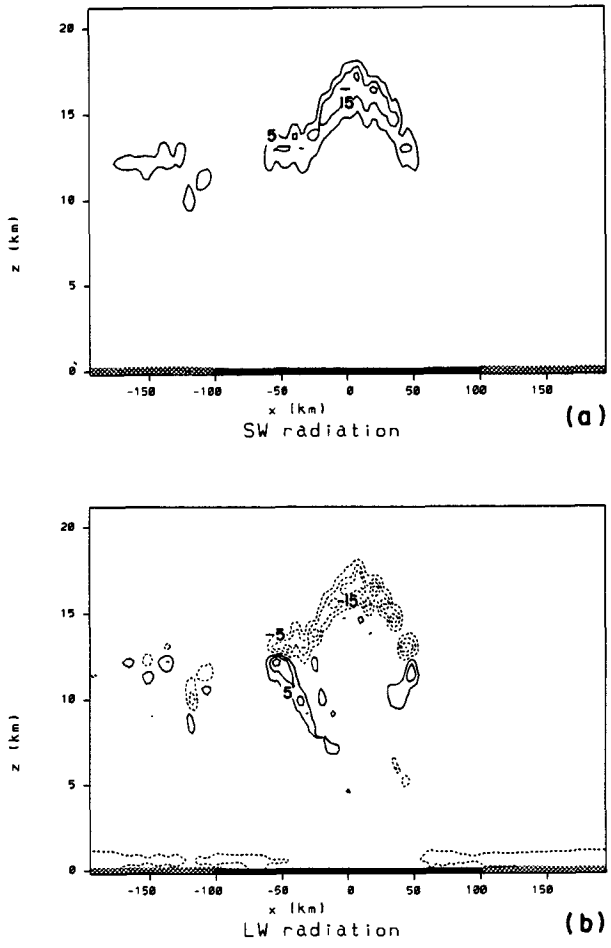

FIG. 19. Radiational heating rate for experiment 3 at 1700 EST (a) Shortwave. (b) Longwave. The contour interval is 10^{-4} °C s^{-1}.

top. By 1800 EST longwave cooling dominates. Compared to latent heating rates, which in the strong updraft region are a few hundred degrees Celcius per day, the radiational heating rates are relatively small. Furthermore, the radiational forcing is not persistent because of the transition from shortwave dominated warming at cloud top to longwave cooling during the late afternoon. For this Type 3 wind profile simulation, the upper-level anvil of pristine ice crystals extends from near the east coast to the left lateral boundary by 2000 EST. Longwave cooling occurs at cloud top and warming at cloud base. In order to determine if radiational effects are playing a significant role in the maintenance of the upper-level anvil, a simulation was initialized at 1800 EST, but with the radiation parameterization turned off at upper levels. At 2000 EST there were no significant differences with the simulation having upper-level radiation turned on. Hence for this short 2-h time scale the parameterized radiational cooling at cloud top and warming at cloud base did not have a significant influence.

5) MOMENTUM TRANSPORTS

If the horizontal momentum equation is integrated across the domain from $-l$ to $+l$ and subgrid-scale diffusion is neglected, we obtain,

$$\frac{\partial}{\partial t}\int_{-l}^{l}\rho_0 u dx = -\frac{\partial}{\partial z}\int_{-l}^{l}\rho_0 uw dx - \rho_0[u^2(l) - u^2(-l)] - [p(l) - p(-l)] + \int_{-l}^{l}\rho_0 fv dx, \quad (3)$$

where the anelastic continuity equation has been used and y derivatives neglected. If the domain size was large enough that the disturbances produced by the convection had not had time to propagate to the lateral boundaries, then for a horizontally homogeneous environment the boundary terms would vanish. Nicholls (1987) found that for a numerically simulated tropical squall line the main contribution to the vertical gradient of the momentum flux came from the convective region. This is also true for the Florida simulations. Also, since the Coriolis term is small, then the vertical gradient of momentum flux probably gives a reasonable estimate of what the net rate of change of momentum at any level would be if the domain was large enough so that the boundary terms could be neglected.

It is important that the momentum transports in downdrafts are considered when calculating the net momentum flux $\int_{-l}^{l}\rho_0 uw dx$, as well as those in updrafts. These may make an important contribution to the net momentum flux and are also important to include when one considers that the storm may be moving relative to the coordinate system. For instance, suppose we have an idealized symmetrical storm (i.e., a vertical updraft with identical compensating subsidence regions on either side) so that in a coordinate system at rest with respect to the storm, the net momentum flux in the updrafts is zero. Now if one measured the net momentum flux in the updrafts in a coordinate system moving with respect to the storm at speed $-c$ it would no longer be zero, but would be $c\int_{-l}^{l}\rho_0 w_{up} dx$. However, there would now be an equal but opposite momentum flux in the downdrafts at any level since the downdraft mass flux equals the upward mass flux. Of course, this assumes that the interval $-l$ to $+l$ is large enough for mass balance to occur. This budget analysis gives a measure of the net momentum tendencies at any level but does not elucidate the dynamical processes responsible for the momentum transports.

The horizontally integrated vertical gradient of the momentum flux is shown in Fig. 20 for experiment 1 (Type 1 wind profile) and for an average in time between 1700–1900 EST. As discussed previously, the main contribution to this term comes from the region of strong convection, so although the convection occurs on the left side of the domain, this does not significantly bias the calculation. Although downdrafts are included in $\int_{-l}^{l}\rho_0 uw dx$ some of the mass balance occurs in the MCR and this may affect the results to a certain extent. The magnitude of the mean momentum flux convergence is considerably smaller than that obtained by Nicholls (1987) for a tropical squall line simulation (see Fig. 11 of that paper; note that results in this case are for a domain average so that they have to be multiplied by the width of the domain for comparison). The largest momentum flux convergences occur near the surface and in the upper troposphere. The sign of these momentum flux convergences is such as to accelerate air from left to right at lower levels and from right to left at upper levels. If a squall line was moving from left to right these would be the correct signs for updraft air flowing from front to rear and downdraft air from rear to front. The system is feeding mostly on low-level air coming from the eastern side of the pen-

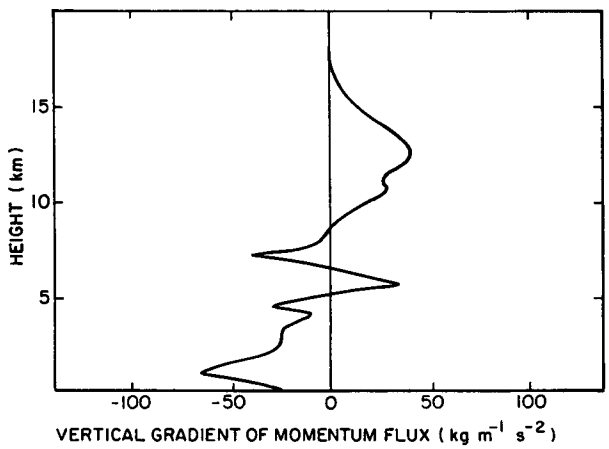

FIG. 20. Vertical gradient of momentum flux.

insula and the upper-level winds cause the anvil to trail to the west, so it has some resemblance to a left to right moving squall line. However, the circulation is more symmetrical than for most squall lines, which usually form in much stronger low-level shear environments and develop updrafts tilted against the shear. The simulations with the Type 3 wind profile and the low-level jet case were more squall-like; nevertheless, none of the simulations in this study produced persistent front to rear flow of the updraft air and rear to front flow of the downdraft air, so momentum flux convergences are comparatively small.

5. Summary and conclusions

The cloud–mesoscale model used in this study appears to be capable of reasonably simulating the broad features of the three characteristic types of systems classified by Blanchard and López (1985). The Type 1 wind profile produces strong convection over the west side of the peninsula. The Type 2 wind profile also produces intense convection over the west side of the peninsula, but nearer the coast, in agreement with observations. However, convection was stronger than observations indicate for Type 2 days. Experiments indicate that the drier midlevel air and more stable lapse rates that typically exist on these days are the main factors responsible for reducing system intensity. The Type 3 wind profile simulation produced strong convection on the east side of the peninsula in agreement with observations. However, convection did not develop earlier than the other two cases and it decayed too soon, before it reached the east coast. Increasing the midlevel moisture (which is typically found on Type 3 days) produced stronger convection earlier in the day, in better agreement with observations, but convection did not last significantly longer. Blanchard and López (1985) note that a 700-mb trough typically exists over north Florida on Type 3 days. Hence, it is possible that synoptic-scale forcing is responsible for the longevity of convection on Type 3 days. These simulations did not produce extensive stratiform-anvil regions in agreement with cloud patterns associated with Florida convection. Relatively shallow anvil clouds in the upper troposphere are quite common, but they typically do not have the vertical depth or longevity of stratiform-anvil clouds associated with tropical or extratropical mesoscale convective systems.

The fairly modest changes to the wind structure made in this study did not result in radically different types of systems forming. Interestingly, the low-level shear case produced an early intense persistent cell, near the center of the peninsula. Nevertheless, most of the rainfall occurred later, over the west side of the peninsula. This would be the expected location of convergence of the oppositely moving sea breezes based on the low-level winds in the absence of convection. The jet profile (experiment 6) momentarily produced a system that resembled a squall line. However, the system lifetime seemed to be too short for it to develop an extensive stratiform region and the pronounced front to rear flowing updraft and rear to front flowing downdraft that is typically associated with squall lines. Hence, momentum transports tended to be relatively small compared to squall lines.

Increasing the low-level temperature and moisture content (experiment 10) led to the earlier development of convection. Sine the convective temperature contrast that can develop, this resulted in a weaker sea breeze. A number of fairly intense cells formed in this simulation and convection was still strong at 2000 EST. The dry soil simulation produced rapidly developing sea breezes that moved inland quickly; whereas the moist soil case produced a much more slowly developing sea breeze. Surprisingly, the total rainfall over the peninsula for the dry soil case was more than for the moist soil. Presumably, this is because the enhanced surface heat fluxes for the dry soil case create stronger low-level convergence over the peninsula to force the convection.

It was noted that shallow cells developed early in the simulations, between the converging sea-breeze fronts. These cells caused heat to be transported upward more rapidly and produced low-level drying and moistening above. As the outer cells developed at the sea-breeze fronts the smaller cells in between were suppressed. These outer cells can have a substantial influence on the propagation speed of the sea-breeze front due to evaporational cooling and water loading (Nicholls et al. 1988) enhancing the pressure gradient across the front. Occasionally, when this early convection is quite strong it is difficult to decide whether the inland moving front is best thought of as a modified sea breeze or as a spreading cold pool. The deep outer cells tended to move with the midlevel winds and to be left behind by the more rapidly moving fronts, which would then initiate one or two new cells as they converged. Typically, one cell near the center of convergence would develop explosively and the outer cells would usually decay, although merger with one of the outer cells occasionally occurred. The initial rapid development was followed by a weakening in intensity, probably due to precipitation falling back into the updraft, and this produced two oppositely traveling gravity waves, having a propagation speed of $\sim$25–30 m s^{-1}. If the convective heating had been steady, one would expect a symmetrical circulation with flow towards the system at low levels and away from it aloft with subsident regions, producing adiabatic warming, propagating away from the convection at $\sim NH/\pi$. A decay in the intensity of convection appears to cause two oppositely moving regions of upward motion (with magnitudes much less than convective updraft velocities) to separate away from the convection. This leads to adiabatic cooling of previously subsided air and forms the two oppositely moving gravity waves. The

rightward moving disturbance for the Type 1 wind profile has the appearance of a clockwise rotating roll. Downward motion at the leading edge of the disturbance produces adiabatic warming and associated pressure perturbations. Upward motion at the back edge leads to adiabatic cooling and an erosion of the disturbance. A considerable amount of the convective energy appears to go into this type of fast-moving mode, which is rapidly propagated away from the peninsula. It is likely that in a more complex three-dimensional situation, the type of roll disturbance found in these two-dimensional simulations will be less well defined.

It has been suggested that the intense cumulonimbus that develops as the sea breezes converge subsequently decays due to precipitation falling back into the updraft. If this is the case it is a classic example of the growth/breakdown process of the Byers and Braham "airmass" thunderstorm model. On the other hand, Tripoli and Cotton (1989a,b) found for a simulation of an orogenic mesoscale system that the first major breakdown was a result of the system moving into a region of mountain-wave-induced subsidence. Subsequent mesoβ-scale regenerations and breakdowns occurred on a 2-h time scale. Their results indicate that these breakdowns were at least partially a consequence of inertial instability. The earth's Coriolis acceleration restricts the scale of divergent response to cumulus heating. This leads to excessive warming of the immediate environment and entrainment of midlevel dry air into the updraft, reducing updraft buoyancy and leading to the breakdown. This is unlikely to be so important for Florida convection, since the Coriolis force is weaker and the system short lived. They also suggest that environmental subsidence warming causes the relative buoyancy within the updraft core to be reduced, contributing to the breakdown. The processes leading to the decay in the intensity of convection and the production of deep oppositely propagating gravity waves requires further investigation.

Rainfall rates observed by Burpee and Lahiff (1984) averaged for all sea-breeze days for June–September from 1973 to 1976 show a peak at 1600 EST. However, for most simulations the rainwater content peaked after 1600 EST. There are several possible explanations for this discrepancy. For instance: 1) Burpee and Lahiff include the southernmost portion of the peninsula in their observations, which is considerably narrower than 200 km; 2) simulations indicate that the timing of intense convection is sensitive to soil moisture content, which has been somewhat arbitrarily specified; and 3) the soil and surface flux parameterizations contain many simplifications. Future simulations should take into account different soil types and vegetation. Further refinement of these parameterizations and testing with observations is needed.

The rainwater content peaked earlier for the moister midlevel simulations in agreement with Burpee and Lahiff's results. However, the total precipitation for the moister midlevel simulations was considerably larger than they obtain for sea-breeze days. Even taking into account that a two-dimensional model probably overestimates rainfall (Nicholls and Weissbluth 1988), results for these moister midlevel simulations still seem large for sea-breeze days and are more like some of the synoptically disturbed days that Burpee and Lahiff observed.

The $Q1$ profile is similar to the profile of latent heat release. At 1500 EST $Q1$ is maximized in the lower troposphere. By 1800 EST this maximum has shifted to the upper troposphere. As convection decays, weak warming occurs aloft and weak cooling below midlevels. Vertical eddy fluxes are an important component of the $Q2$ budget as found by Lafore et al. (1988) for a tropical squall line. During the deep convective stage, large-scale drying occurs, which is maximized at low-levels. Although the temperature profile through the strong updraft region shows that it approaches a moist adiabat aloft, consistent with a parcel lifted from near the surface, subsidence outside the cloud produced warming substantially less than this. By evening the horizontally averaged thermodynamic profile was very similar to the sounding used to initialize the model. Although, to a certain extent this reflects the lateral boundary conditions that cause the inflow to tend towards the initial state, it also is a consequence of the rapid movement out of the region of the deep gravity mode that contains much of the convective energy.

The net radiational heating at cloud top underwent a transition from warming during the midafternoon to cooling during the early evening. This change in sign of the heating and its relatively small magnitude compared to latent heating rates indicates that its effect on the dynamics of the system was quite small. Initializing the Type 3 wind profile case at 1800 EST, but with upper-level radiational effects eliminated, produced no significant differences at 2000 EST with the simulation having radiation turned on.

An interesting aspect of the no-wind simulation was that the rainfall distribution was skewed to the west side of the peninsula. Hence, the introduction of small randomly specified temperature perturbations ($<0.2°C$) into the first level above the surface had a significant influence on the final rainfall distribution. In order to test this sensitivity further, an additional simulation was carried out for the Type 1 wind profile using a different set of random numbers (note for all the previous experiments the same set of random numbers was used). This case produced deep, weak convection at both sea-breeze fronts simultaneously, unlike experiment 1. Similarly to experiment 1, rapid convective development occurred at 1600 EST, leading to a peak in rainwater content just after 1700 EST. However, it did not produce a stronger secondary peak at 1830 EST, but instead a weaker secondary peak occurs at 1930 EST. The accumulated rainfall distributions were similar, although the peak was located ~ 10

km to the west of experiment 1, which is consistent with the initial development of deep convective cells at both sea-breeze fronts. Therefore, there is some sensitivity to small variations of the initial conditions, which is disconcerting as far as the ability to predict these events is concerned. On the other hand, there were some strong controls on convective development. In particular, most of the rainfall in these simulations almost always occurred near the location that the oppositely moving sea breezes would have converged in the absence of any moist convection.

These two-dimensional simulations provide a basis for future, more complex three-dimensional simulations that will include the effects of an irregular coastline, Lake Okeechobee, and directional wind shear. Convectively explicit simulations of Florida convection provide a valuable test bed for evaluating convective parameterization schemes, particularly where the complexities associated with mesoscale stratiform-anvil cloud and synoptic-scale baroclinicity are absent. Diagnostic comparisons of apparent heating and moistening rates are being made with those predicted by cumulus parameterization schemes (e.g., Kuo 1974; Fritsch and Chappell 1980) as well as prognostic evaluations, and will be reported on in a future paper. There is a clear need for more observational studies of convective systems in the Florida region. Detailed case studies of particular convective events are not presently available to compare with model results. Microphysical observations at the upper-levels of convective storms are particularly sparse and model results are fairly sensitive to some of the assumed parameters. For instance, decreasing the initial mass of pristine ice crystals and the fall speed of snow (which, at present, uses the rimed hexagonal plate distribution of Locatelli and Hobbs 1974) produces significantly larger anvils than occur for the present choice of variables. There is a considerable margin of uncertainty for many of the microphysical parameters, which observational studies may help to reduce.

Acknowledgments. The authors are grateful to Craig Tremback, Robert Walko, and Gregory Tripoli for the very helpful computational assistance they provided. Discussions with Jenn-Luen Song, Moti Segal, and Hans Verlinde are much appreciated. We would like to thank Jim Purdom for providing the satellite picture. Thanks to Dallas McDonald and Tony Smith for preparing this manuscript.

This research has been supported by the National Aeronautics and Space Administration under Grant NAG5-359, and the Army Research Office under Contract DAAL03-86-K-0175.

REFERENCES

Balaji, V., and T. L. Clark, 1988: Scale selection in locally forced convective fields and the initialization of deep cumulus. *J. Atmos. Sci.*, **45**, 3212–3235.

Blanchard, D. O., and R. E. Lopez, 1985: Spatial patterns of convection in south Florida. *Mon. Wea. Rev.*, **113**, 1282–1299.

Burpee, R. W., and L. N. Lahiff, 1984: Area-average rainfall variations on sea-breeze days in south Florida. *Mon. Wea. Rev.*, **112**, 510–519.

Byers, H. R., 1965: *Elements of Cloud Physics.* University of Chicago Press,

——, and H. R. Rodebush, 1948: Causes of thunderstorms of the Florida peninsula. *J. Meteor.*, **5**, 275–280.

Chen, C., and W. R. Cotton, 1983: A one-dimensional simulation of the stratocumulus-capped mixed layer. *Bound.-Layer Meteor.*, **25**, 289–321.

Clark, T. L., T. Hauf and J. P. Kuettner, 1986: Convectively forced interval gravity waves: results from two-dimensional experiments. *Quart. J. Roy. Meteor. Soc.*, **112**, 899–926.

Cooper, H. J., 1981: The behaviour of surface wind and thermodynamic fields in the presence of deep convection. Ph.D. dissertation, University of Virginia, Charlottesville, 392 pp.

——, M. Garstang and J. Simpson, 1982: The diurnal interaction between convection and peninsular-scale forcing over south Florida. *Mon. Wea. Rev.*, **110**, 486–503.

Cotton, W. R., M. A. Stephens, T. Nekhkorn and G. J. Tripoli, 1982: The Colorado State University three-dimensional cloud–mesoscale model—1982: Part II: An ice parameterization. *J. Rech. Atmos.*, **16**, 295–320.

Cunning, B., and M. DeMaria, 1986: An investigation of the development of cumulonimbus systems over south Florida. Part I: Boundary layer interactions. *Mon. Wea. Rev.*, **114**, 5–24.

Fletcher, N. H., 1962: *Physics of Rain Clouds.* Cambridge University Press, 386 pp.

Frank, N. L., P. L. Moore and G. E. Fisher, 1967: Summer shower distribution over the Florida peninsula as deduced from digitized radar data. *J. Appl. Meteor.*, **6**, 309–316.

Fritsch, J. M., and C. F. Chappell, 1980: Numerical prediction of convectively driven mesoscale pressure systems. Part I: Convective parameterization. *J. Atmos. Sci.*, **37**, 1722–1733.

Gentry, R. C., and P. L. Moore, 1954: Relation of local and general wind interaction near the sea coast to time and location of airmass showers. *J. Meteor.*, **11**, 507–511.

Gordon, G. L., and J. D. Marwitz, 1981: Secondary ice crystal production in stable orographic clouds over the Sierra Nevada. *Proc., Eighth Conference on Inadvertent and Planned Weather Modification,* Amer. Meteor. Soc., Reno, 62–63.

Hill, G. E., 1974: Factors controlling the size and spacing of cumulus clouds as revealed by numerical experiments. *J. Atmos. Sci.*, **31**, 646–673.

Huffman, P. J., and G. Vali, 1973: The effect of vapor depletion on ice nucleus measurements with membrane filters. *J. Appl. Meteor.*, **12**, 1018–1024.

Johnson, R. H., 1976: The role of convective-scale precipitation downdrafts in cumulus and synoptic-scale interactions. *J. Atmos. Sci.*, **33**, 1890–1910.

Klemp, J. B., and D. K. Lilly, 1978: Numerical simulation of hydrostatic mountain waves. *J. Atmos. Sci.*, **35**, 78–107.

——, and R. B. Wilhelmson, 1978: The simulation of three-dimensional convection storm dynamics. *J. Atmos. Sci.*, **35**, 1070–1096.

Kuo, H. L., 1974: Further studies of the parameterization of the influence of cumulus convection on large-scale flow. *J. Atmos. Sci.*, **31**, 1232–1240.

Locatelli, and Hobbs, 1974: Fallspeeds and masses of solid precipitation particles. *J. Geophys. Res.*, **79**, 2185–2197.

Lafore, J-P., J-L. Redelsperger and G. Jaubert, 1988: Comparison between a three-dimensional simulation and Doppler radar data of a tropical squall line: transports of mass, momentum, heat, and moisture. *J. Atmos. Sci.*, **45**, 3483–3500.

Louis, J. F., 1979: A parametric model of vertical eddy fluxes in the atmosphere. *Bound. Layer Meteor.*, **17**, 187–202.

Ludlam, F. H., 1980: *Clouds and Storms: The Behavior and Effect of Water in the Atmosphere.* Pennsylvania State University Press.

Manton, M. J., and W. R. Cotton, 1977: Parameterization of the atmospheric surface layer. *J. Atmos. Sci.*, **34**, 331–334.

McCumber, M. C., and R. A. Pielke, 1981: Simulation of the effects of surface fluxes of heat and moisture in a mesoscale numerical model—Part 1: Soil layer. *J. Geophys. Res.*, **86**, 9929–9938.

Nicholls, M. E., 1987: A comparison of the results of a two-dimensional simulation of a tropical squall line with observations. *Mon. Wea. Rev.*, **115**, 3055–3077.

——, and M. J. Weissbluth, 1988: A comparison of two-dimensional and quasi-three-dimensional simulations of a tropical squall line. *Mon. Wea. Rev.*, **116**, 2437–2452.

——, R. H. Johnson and W. R. Cotton, 1988: The sensitivity of two-dimensional simulations of tropical squall lines to environmental profiles. *J. Atmos. Sci.*, **45**, 3625–3649.

Pielke, R. A., 1974: A three-dimensional numerical model of the sea breezes over south Florida. *Mon. Wea. Rev.*, **102**, 115–139.

——, and W. R. Cotton, 1977: A mesoscale analysis over south Florida for a high rainfall event. *Mon. Wea. Rev.*, **105**, 343–362.

——, and Y. Mahrer, 1978: Verification analysis of the University of Virginia three-dimensional mesoscale model prediction over south Florida for July 1, 1973. *Mon. Wea. Rev.*, **106**, 1568–1589.

Pruppacher, H. R., and J. D. Klett, 1978: *Microphysics of Clouds and Precipitation.* D. Reidel Publishing Company, 714 pp.

Rossby, C. G., 1938: Mutual adjustment of pressure and velocity distributions in certain simple current systems. *J. Mar. Res.*, **II**, 239–263.

Rotunno, R., J. B. Klemp and M. L. Weisman, 1988: A theory for strong, long-lived squall lines. *J. Atmos. Sci.*, **45**, 463–485.

Schwartz, B. E., and L. F. Bosart, 1979: The diurnal variability of Florida rainfall. *Mon. Wea. Rev.*, **107**, 1535–1545.

Song, J.-L., 1986: A numerical investigation of Florida's sea breeze–cumulonimbus interactions. Ph.D. dissertation, Colorado State University, Fort Collins, Colorado, 187 pp.

Stephens, G. L., 1978a: Radiation profiles in extended water clouds. I: Webster theory. *J. Atmos. Sci.*, **35**, 2111–2122.

——, 1978b: Radiation profiles in extended water clouds. II: Parameterization schemes. *J. Atmos. Sci.*, **35**, 2123–2132.

Tremback, C. J., and R. Kessler, 1985: A surface temperature and moisture parameterization for use in mesoscale numerical models. Preprints, *Seventh Conference on Numerical Weather Prediction,* Montreal, Amer. Meteor. Soc., 17–20.

Tripoli, G. J., and W. R. Cotton, 1980: A numerical investigation of several factors contributing to the observed variable intensity of deep convection over south Florida. *J. Appl. Meteor.*, **19**, 1037–1063.

——, and W. R. Cotton, 1982: The Colorado State University three-dimensional cloud–mesoscale model—1982. Part I: General theoretical framework and sensitivity experiments. *J. Rech. Atmos.*, **16**, 185–220.

——, and W. R. Cotton, 1989a: Numerical study of an observed orogenic mesoscale convective system. Part I: Simulated genesis and comparison with observations. *Mon. Wea. Rev.*, **117**, 273–304.

——, and W. R. Cotton, 1989b: Numerical study of an observed orogenic mesoscale convective system. Part II: Analysis of governing dynamics. *Mon. Wea. Rev.*, **117**, 305–328.

Ulanski, S. L., and M. Garstang, 1978: The role of surface divergence and vorticity in the life cycle of convective rainfall. Part I: Observation and analysis. *J. Atmos. Sci.*, **35**, 1047–1062.

Yanai, M., S. Esbensen and J. Chu, 1973: Determination of bulk properties of tropical cloud clusters from large-scale heat and moisture budgets. *J. Atmos. Sci.*, **30**, 611–627.